



University of Oxford

Hertford College



# The C-Band All Sky Survey

Submitted in fulfillment of the requirements for the award of a D.Phil  
at the University of Oxford

presented by Charles Copley  
supervised by Professor Michael Jones

August 22, 2012

# Contents

<b>1</b>	<b>Introduction</b>	<b>1</b>
1.1	Science Goals . . . . .	1
1.2	. . . . .	1
1.3	Foreground Removal Techniques . . . . .	1
1.4	Survey Requirements . . . . .	2
1.4.1	Beam Size . . . . .	2
1.4.2	Confusion Limit . . . . .	2
<b>2</b>	<b>Overview of the C-BASS Project</b>	<b>3</b>
2.1	Northern Antenna . . . . .	3
2.1.1	Optical Configuration . . . . .	3
2.1.2	The Analogue Radiometer/Polarimeter . . . . .	4
2.1.3	Survey Environment . . . . .	4
2.1.4	State of Survey . . . . .	4
2.2	Southern Antenna . . . . .	4
2.2.1	Optical Configuration . . . . .	4
2.2.2	The Digital Radiometer/Polarimeter . . . . .	4
2.2.3	State of Survey . . . . .	4
2.3	Notch Filters . . . . .	5
2.3.1	Radio Frequency Interference (RFI) . . . . .	5
2.3.2	Filter Design . . . . .	10
2.3.3	Specifications . . . . .	10
2.3.4	Design . . . . .	10
2.3.5	Manufacture and Testing . . . . .	12
2.3.6	Cooling the Filters . . . . .	14
2.3.7	Filter Installation at Owens Valley Antenna . . . . .	15
2.3.8	Other Possibilities . . . . .	15
<b>3</b>	<b>The Southern Receiver and Component Designs</b>	<b>17</b>
3.1	Motivation . . . . .	17
3.1.1	Block Diagram . . . . .	17

3.1.2	Designs Choices . . . . .	20
3.1.3	Passive Component Insertion Loss . . . . .	20
3.2	Digital Hardware . . . . .	23
3.2.1	Roach . . . . .	23
3.2.2	iADC . . . . .	23
3.3	Low Frequency Filters . . . . .	23
3.3.1	Filter Design . . . . .	24
3.3.2	Component Choices . . . . .	27
3.3.3	Manufacture Techniques and Packaging . . . . .	27
3.3.4	Performance . . . . .	31
3.4	Double Sideband Mixers . . . . .	31
3.4.1	Design and Component Choice . . . . .	31
3.4.2	Performance . . . . .	31
3.5	DC-6GHz Amplifiers . . . . .	31
3.5.1	Performance . . . . .	32
3.5.2	Component Choice . . . . .	32
3.5.3	Wideband Biasing Chokes . . . . .	32
3.5.4	DC Blocking Capacitors . . . . .	32
3.6	Low Noise Amplifier Power Supply . . . . .	33
<b>4</b>	<b>Receiver Testing</b>	<b>36</b>
4.1	Introduction . . . . .	37
4.1.1	Order of Components . . . . .	37
4.2	Load Stabilisation . . . . .	37
4.2.1	Cryocontrol . . . . .	37
4.2.2	Bobbin Redesign . . . . .	37
4.2.3	Temperature Sensor . . . . .	37
4.3	RF and IF Band Definitions . . . . .	37
4.3.1	System Temperature . . . . .	37
4.4	2-20GHz Amplifier System Tests . . . . .	37
4.4.1	System Temperature . . . . .	37
4.5	DC-4GHz Amplifiers . . . . .	37
4.5.1	Wideband Capacitors . . . . .	37
4.5.2	Wideband Biasing Choke . . . . .	37
4.6	Horn Tests . . . . .	37
4.6.1	Anechoic Chamber Measurements . . . . .	37
4.7	Full System Tests . . . . .	37
4.7.1	Low Noise Amplifiers (LNA) . . . . .	37
4.7.2	Cold Component Tests . . . . .	37
4.8	Design Improvements over Northern Frontend . . . . .	37
4.8.1	SuperSMA connectors . . . . .	37

4.8.2	Redesign RF route . . . . .	37
4.8.3	Thermal decoupling of temperature Load . . . . .	37
<b>5</b>	<b>The Southern C-BASS System</b>	<b>38</b>
5.1	System Diagram . . . . .	39
5.1.1	Self-generated RFI considerations . . . . .	39
5.1.2	Remote Operations . . . . .	39
5.2	Servo Control . . . . .	39
5.2.1	Description . . . . .	39
5.3	Primary Dish Profile . . . . .	39
5.3.1	Photogrammetry . . . . .	39
5.4	Site Establishment . . . . .	44
5.4.1	Infrastructure . . . . .	44
5.4.2	Science Requirements . . . . .	44
<b>6</b>	<b>Deploying the Southern Receiver</b>	<b>47</b>
6.1	Strategy . . . . .	47
6.2	Commissioning Observations . . . . .	47
6.2.1	Beam Patterns . . . . .	47
6.2.2	System Temperature . . . . .	47
6.2.3	Power Spectra . . . . .	47
<b>7</b>	<b>Preliminary Data (if possible)</b>	<b>48</b>
7.1	Science Project . . . . .	48
7.1.1	TBD:Galactic Centre?Spinning Dust Regions? deep CMB fields? . . . . .	48
7.1.2	Data Reduction . . . . .	48
7.1.3	Data Analysis . . . . .	48
<b>8</b>	<b>Conclusions</b>	<b>49</b>
8.1	What's been done . . . . .	49
8.2	What remains . . . . .	49
.1	Stokes Parameters . . . . .	50
.2	Pseudo-correlation architecture . . . . .	51
.3	Digital Implementation . . . . .	53
.3.1	Advantages of the Digital Implementation . . . . .	53

## Abstract

The C-Band All Sky Survey (C-BASS) is a survey of the sky foreground in both intensity and polarisation at a frequency of 5 GHz with a resolution of  $\approx 0.8^\circ$ . Northern and Southern sky coverage is provided by antennas located at the Owens Valley Radio Observatory (OVRO) in California, and the *MeerKAT* support base in South Africa, respectively.

The primary science goal is to provide a C-Band all sky intensity and polarisation map to augment the WMAP surveys. This lower frequency constraint will allow improved foreground subtraction in Cosmic Microwave Background (CMB) experiments. Removal of foreground contamination will place a limit on the success of CMB experiments that attempt to detect the B-Mode polarisation of the CMB.

This report details the technical developments of the experiment (both North and Southern surveys), the status of the Northern sky survey, and provides details of the new digital receiver being designed and built to deploy on the South African telescope.

# Chapter 1

## Introduction

### 1.1 Science Goals

### 1.2

### 1.3 Foreground Removal Techniques

The beginnings CMB polarization studies focused on measuring the relatively bright E-Mode power spectrum. Small area surveys conveniently provided sufficient signal to detect both EE and TE polarization (Leitch & Kovac 2005, Mcmahon et al. 2005, Barkats et al. 2005, Readhead et al. 2004) , and areas obfuscated by foregrounds were avoided. Detecting the much fainter B-Mode signals, will require larger area surveys and galactic foreground contamination will be unavoidable (Tegmark et al. 2003). This will require foreground removal.

A number of different foreground removal techniques exist.  
(Hansen & Banday 2006),(Delabrouille & Cardoso 2009),(Leach & Cardoso 2008),(Armitage-Caplan 2011),(Gold et al. 2009),(Dunkley et al. 2009),

## 1.4 Survey Requirements

### 1.4.1 Beam Size

$$\theta_{HPBW} \approx \frac{1.2\lambda}{D} \quad (1.1)$$

$$\theta_{HPBW} \approx 0.68^\circ \quad (1.2)$$

$$\theta_{HPBW} \approx 41'' \quad (1.3)$$

### 1.4.2 Confusion Limit

At centimetre wavelengths the confusion noise ( $\sigma_c$ ) is observed to be given by

$$\sigma_c \approx 0.2(\nu)^{-0.7}(\theta_{HPBW})^2 \quad (1.4)$$

$$\sigma_c \approx 533mJy/beam \quad (1.5)$$

where the  $\sigma_c$  is the confusion noise (mJ/Beam),  $\nu$  is in GHz and  $\theta_{HPBW}$  in arcminutes

<http://www.atnf.csiro.au/research/radio-school/2011/talks/CondonContinuum2011.pdf>

<http://www.cv.nrao.edu/course/astr534/Radiometers.html>

The confusion limit is about  $5\sigma_c$  or  $\approx 2.5$  Jy

# **Chapter 2**

## **Overview of the C-BASS Project**

(Condon n.d.)

### **2.1 Northern Antenna**

#### **2.1.1 Optical Configuration**

Gregorian optical configuration

### **2.1.2 The Analogue Radiometer/Polarimeter**

### **2.1.3 Survey Environment**

### **2.1.4 State of Survey**

## **2.2 Southern Antenna**

### **2.2.1 Optical Configuration**

### **2.2.2 The Digital Radiometer/Polarimeter**

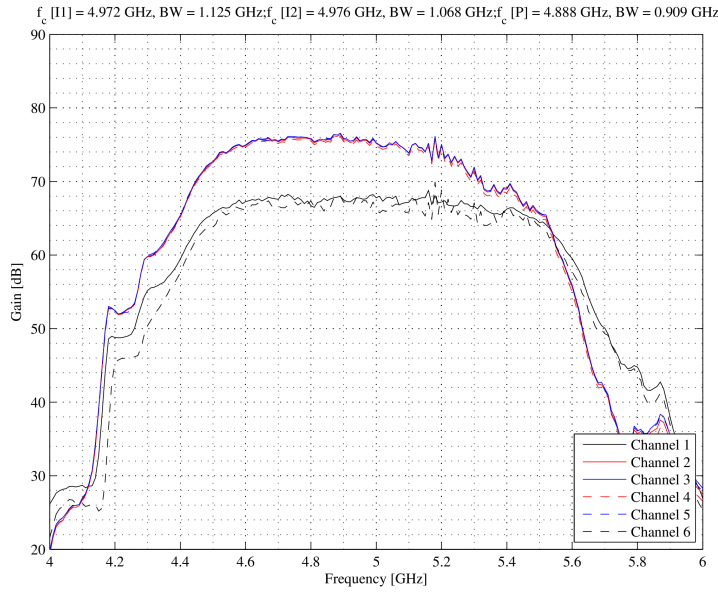
### **2.2.3 State of Survey**

## 2.3 Notch Filters

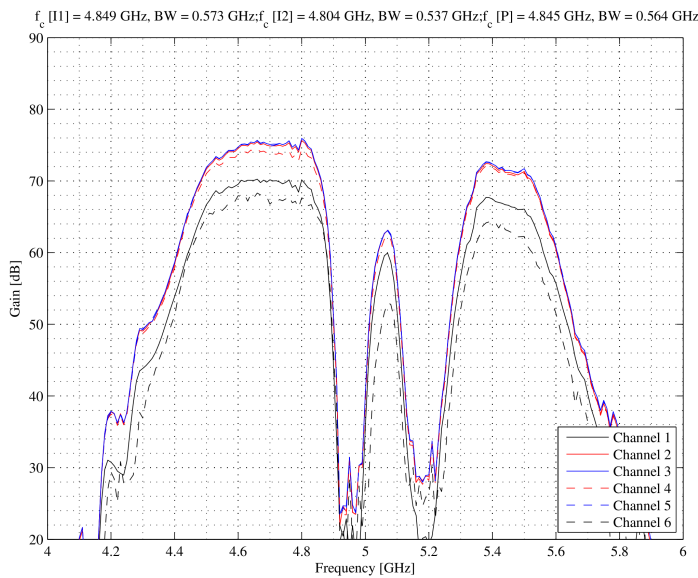
### 2.3.1 Radio Frequency Interference (RFI)

Unfortunately, as the survey has progressed, we have become increasingly beset by terrestrial, satellite and aircraft interference (see Figure 2.2). Aircraft interference is sporadic enough in nature to flag out, but satellite and terrestrial interference is, however, more troublesome (see Figure 2.2). The effect on the data is noticeable up to 50° elevation, making post-measurement removal very difficult, if not impossible.

To remedy this on the Northern receiver, we designed a set of narrowband notch filters (to reduce the effect of in-band RFI) and also increased the out-of band attenuation, by adding a second stage of band-defining filters. The resulting change of the passband can be seen in Figure 2.1. The effect on data quality (Figure 2.3) is noticeable and, with the 0.25s/pixel integration period used to produce these scans, RFI is no longer noticeable.



(a) The C-BASS pass band before installing any additional filtering



(b) The C-BASS pass band after installing the Notch filters and additional Band pass filters

Figure 2.1: C-BASS passband changes

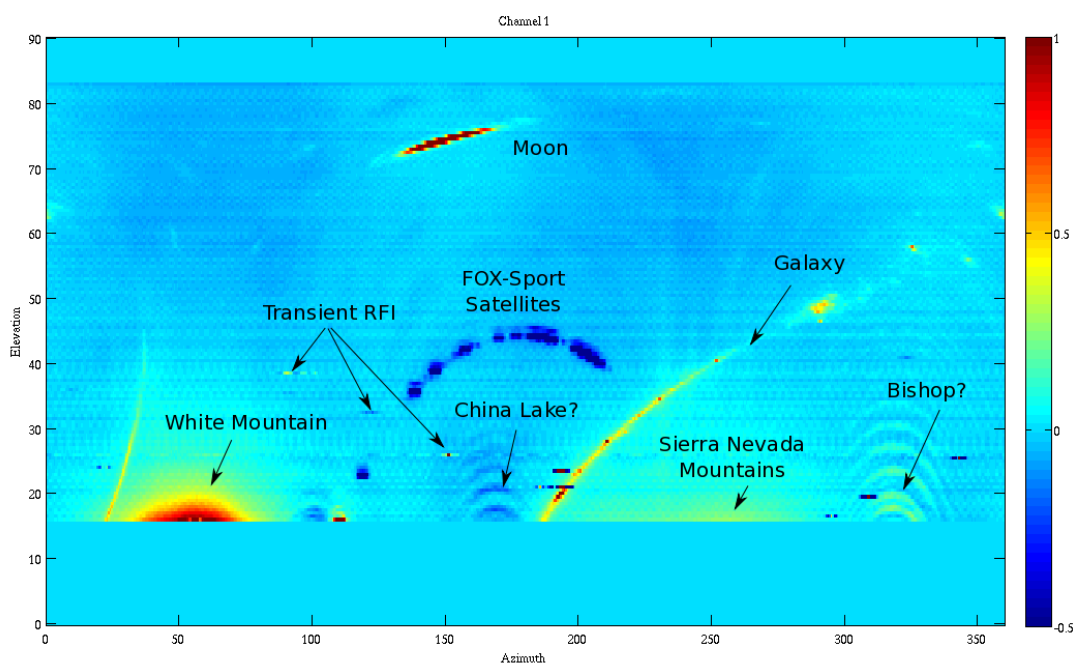
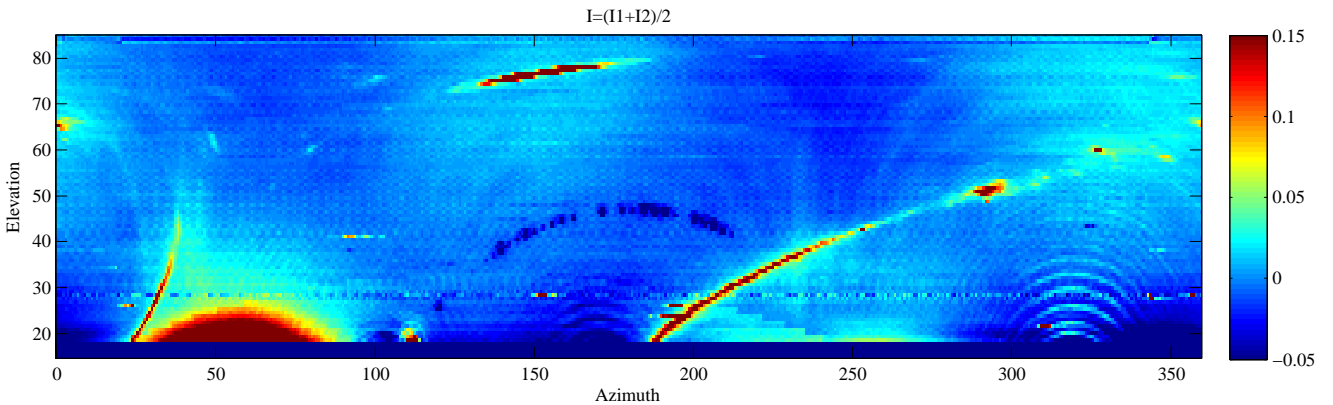
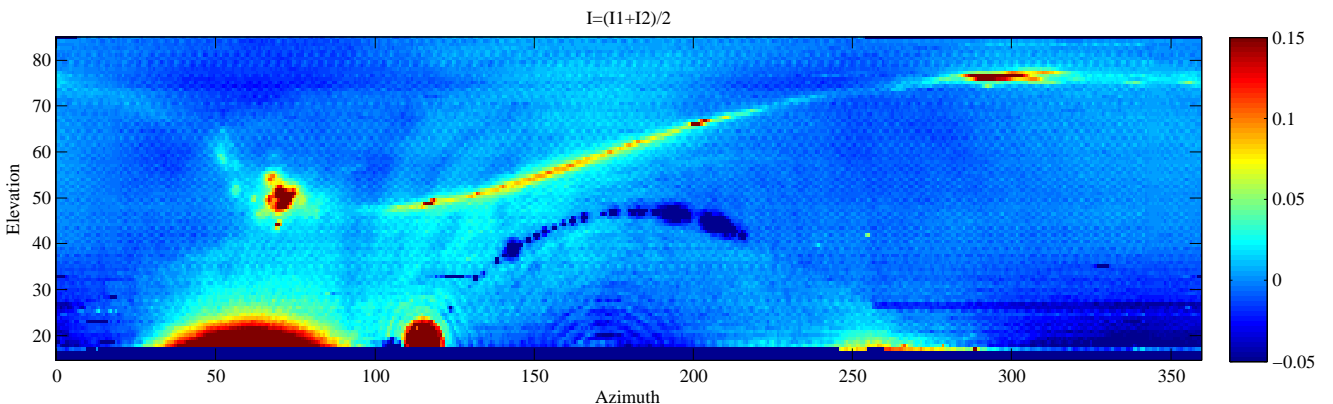


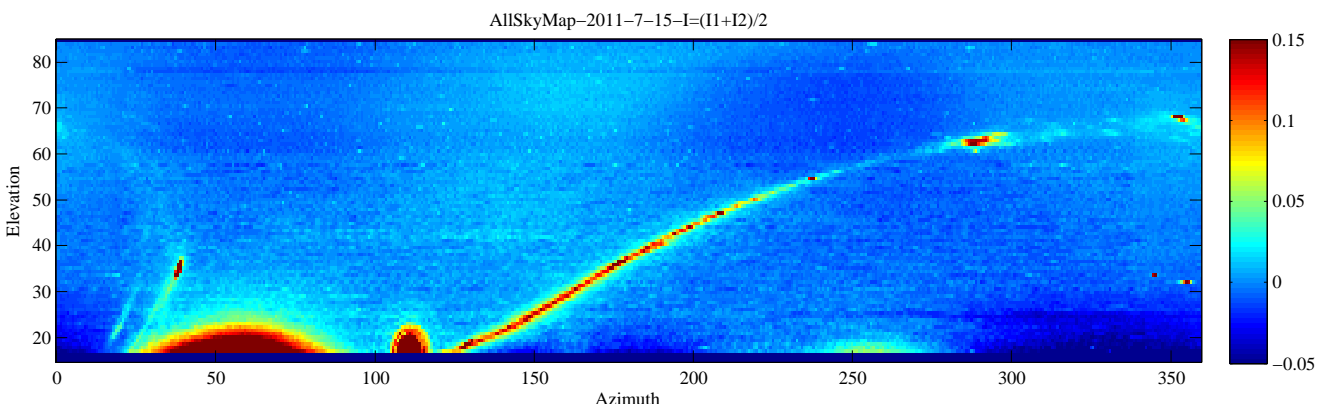
Figure 2.2: Annotated Intensity map (courtesy Oliver) of the sky as seen by the Owens Valley C-BASS antenna. Note the elevation extent of the diffraction patterns seen as a result of the terrestrial radiation



(a) Sky before the installation of notch filters. Note the diffraction patterns produced by strong RFI sources detected in the antenna sidelobes

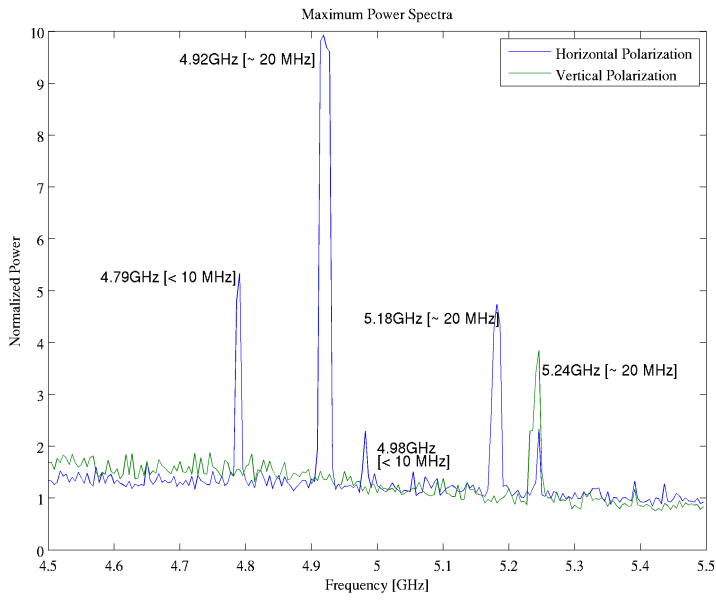


(b) Sky after the installation of notch filters. All terrestrial RFI aside from a strong source to the South ( $180^\circ$  Azimuth) has been removed

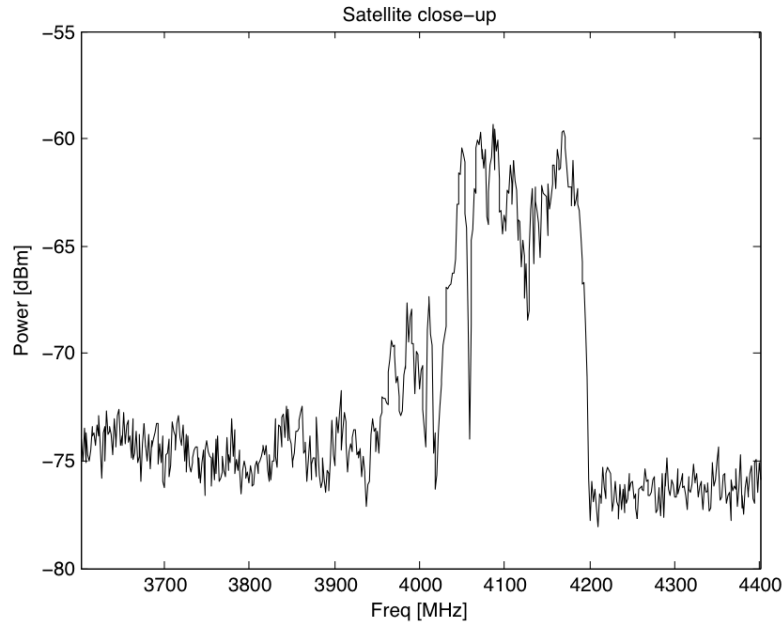


(c) Sky after the installation of notch filters and additional band pass filters. All terrestrial radiation removed, and geostationary satellites are no longer visible

Figure 2.3: Installing additional filtering: These images show the dramatic improvement in data quality brought about by the addition of notch filters and additional band defining filters in the E-BASS RF path



(a) Radio Frequency Interference as captured by a spectrum analyser attached to the output of the C-BASS cryostat. We think the 4.79 GHz spike is sporadic and does not require filtering



(b) Spectra of geostationary satellites

Figure 2.4

### 2.3.2 Filter Design

### 2.3.3 Specifications

An obvious solution to this is to design a set of very high Q ( $Q = \frac{f_c}{\Delta f}$ ) notch filters. A cursory examination of Figure 2.4 suggests that each RFI band is approximately 25 MHz wide, which at 5 GHz requires a Q of 200. This is a challenging task.

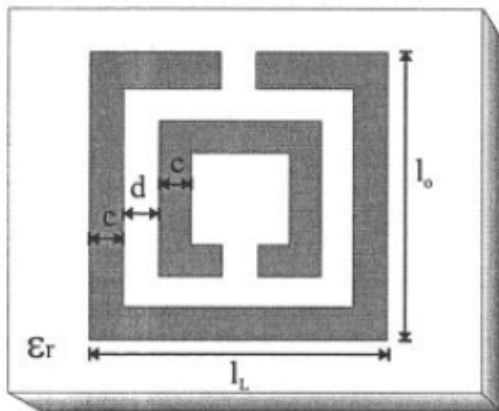
However upon more careful examination of Figure 2.4, it is clear that some relaxation of this is possible. Each of the major RFI bands (i.e 4.92 GHz and 5.18 GHz) has a second proximate RFI peak, which could be included into a single notch filter. To attenuate both of these a stop band of 80 MHz is required. This is an achievable goal.

### 2.3.4 Design

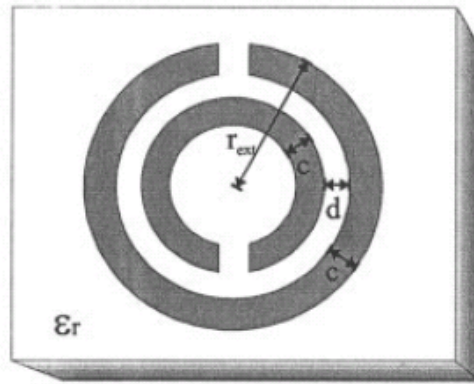
High Q filter design using microstrip, is usually accomplished using resonance structures placed parallel to a microstrip transmission line, with electromagnetic coupling between the two. The dimensions of these structures can be adjusted to resonate at the frequency of interest. Alternatively band pass filters can be constructed in a similar fashion by placing these resonating structures in series with the transmission line.

Since this was our first foray into the world of resonance filter designs we looked for a simple resonating structure which would be easy to 'tune'. The design we chose (Garcia-Garcia et al. 2005) is shown in Figure 2.5.

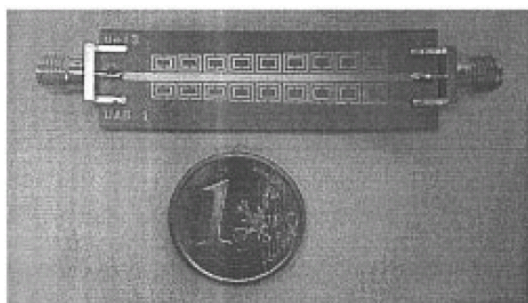
We used these resonators to design 3 initial filters for 4.65 GHz, 4.70 GHz and 4.75 GHz. This we felt would allow use to check that the filter behaved as the simulations predicted across a small range of frequencies.



(a) Square Resonator



(b) Circular Resonator



(c) Manufactured Bandstop filter with a series of differently tuned square resonator structures

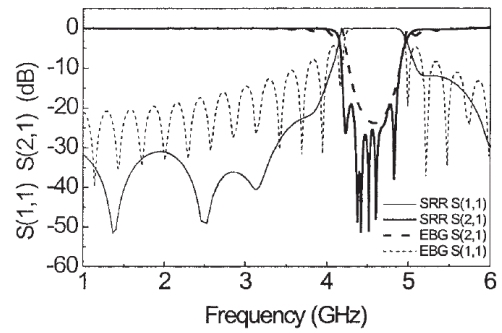


Figure 2.5: Possible resonance structures for the notch filter (Garcia-Garcia et al. 2005). These diagrams show the dimensions that can be adjusted. We chose to pursue the square type resonance structure 2.5a

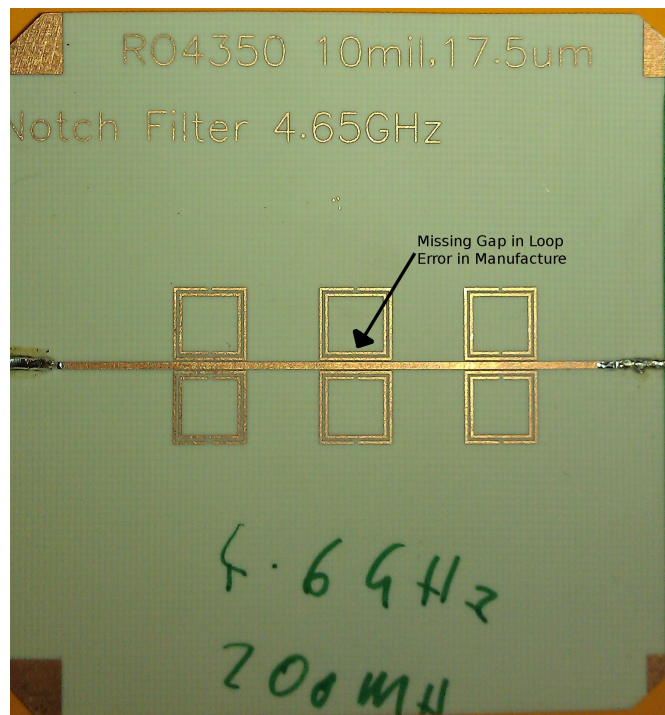


Figure 2.6: The manufactured 4.65 GHz notch filter. Used Rogers RO4350 10mil ( $\epsilon_r=3.66$ ) with 17.5um Copper layers for manufacture. Note the error in manufacture. This produced an additional notch feature (apparent in Figure 2.7) at 10% higher frequency than the central notch feature. This has been corrected

### 2.3.5 Manufacture and Testing

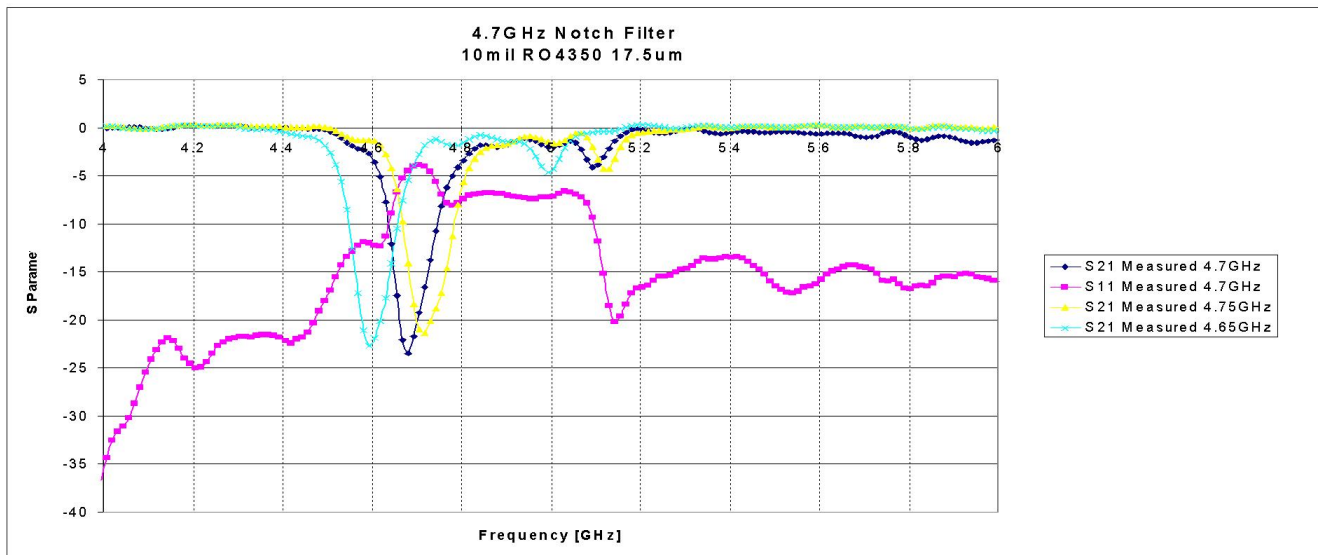


Figure 2.7: Measured Results of the three square ring resonator structures. We see the additional feature 10% higher in frequency caused by the error in manufacture (see Figure 2.6) in all three of the designs. We also see that the central notch behaves as we expect although they are approximately 50 MHz lower than the simulations predict

### 2.3.6 Cooling the Filters

We expected the filter bandwidth to improve at lower temperatures, since most of the loss was resistive loss in the Copper. To test this we initially cooled the design with liquid nitrogen, however we found that the liquid nitrogen effected the central response by changing the dielectric constant of the region directly above the resonator structures.

We decided then to conduct the test in the Oxford test cryostat and achieved the following results.

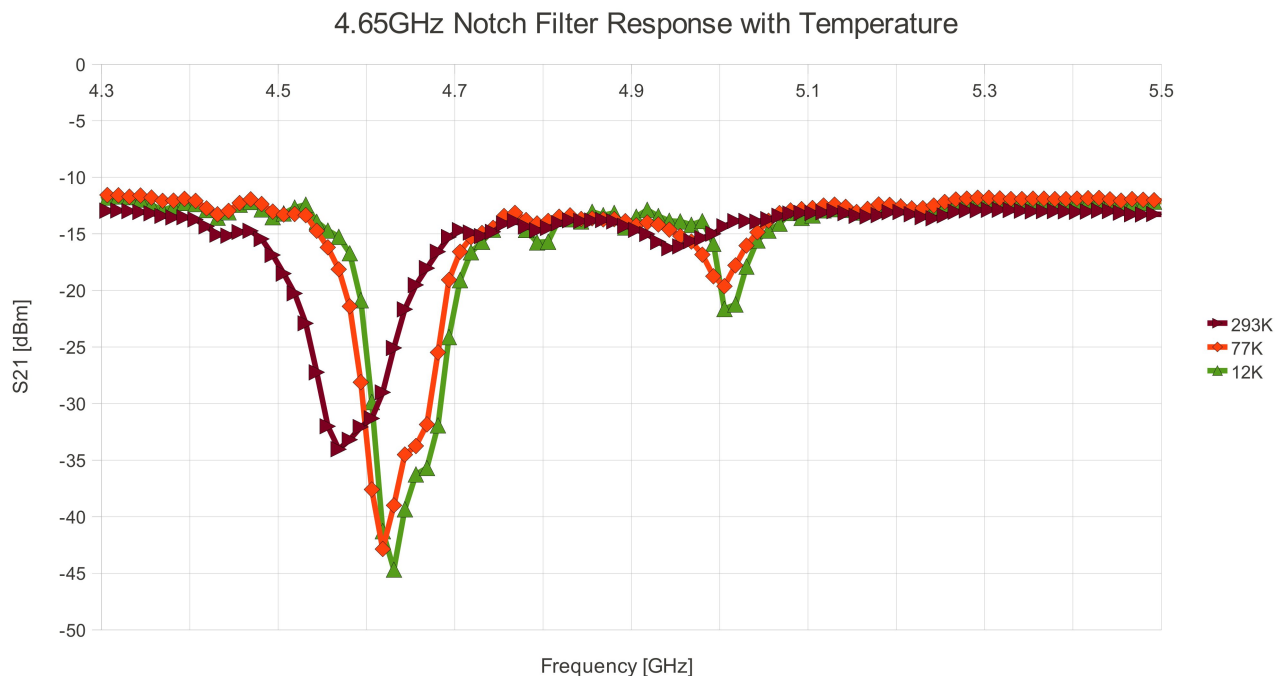


Figure 2.8: Cooling the Filter in the test cryostat. Note the additional notch feature becomes more pronounce when cooled.

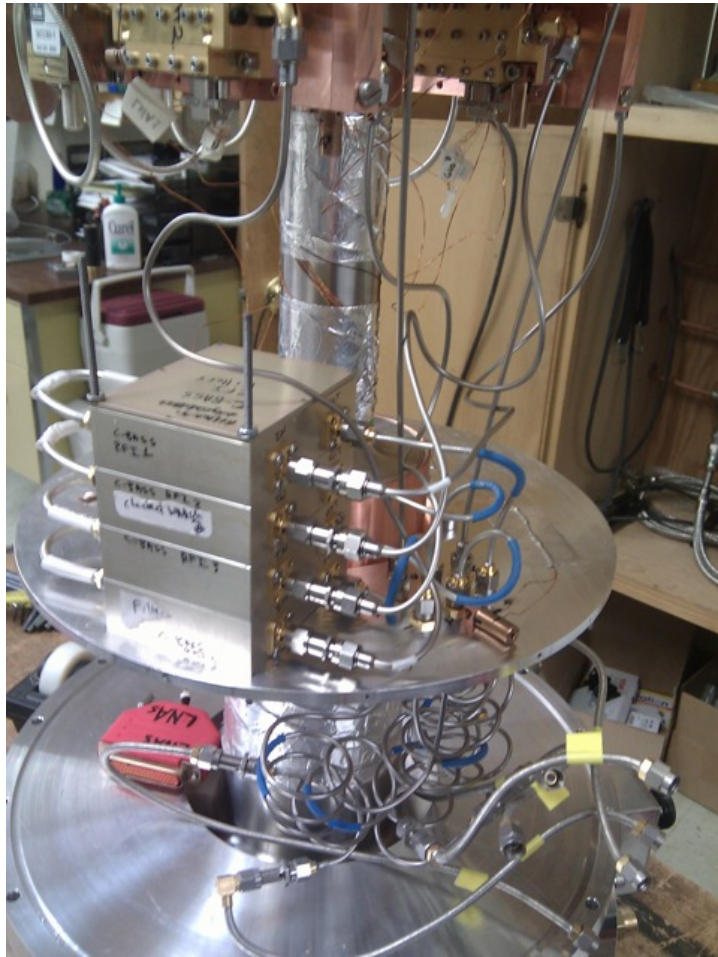


Figure 2.9: The notch filters installed in the cryostat at Owens Valley

### 2.3.7 Filter Installation at Owens Valley Antenna

The RFI notch filters were installed at the Owens Valley antenna on the 7 May 2011 (see Figure 2.9). The filters have successfully suppressed the RFI shown in Figure 2.4. The transmission through the cryostat can be seen in Figure 2.10.

### 2.3.8 Other Possibilities

High temperature superconducting filters (Futatsumori et al. 2008), would achieve much higher Q values, allowing us to design filters for each of the RFI features. However the manufacture process

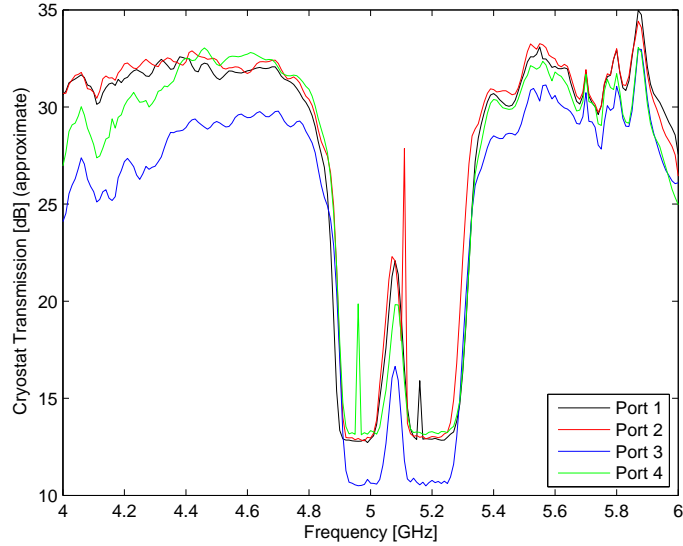


Figure 2.10: Transmission through the cryostat after the installation of the notch filters. The two stop bands prevent incoming RFI from contaminating the signal

is complicated, and in addition would be a new method for the Physics department. In addition, the frequency distribution of the four RFI signals obviate any significant advantage of higher Q filters.

The other possibility is to switch over to a digital polarimeter, a clone of the new Southern receiver.

# **Chapter 3**

## **The Southern Receiver and Component Designs**

### **3.1 Motivation**

#### **3.1.1 Block Diagram**

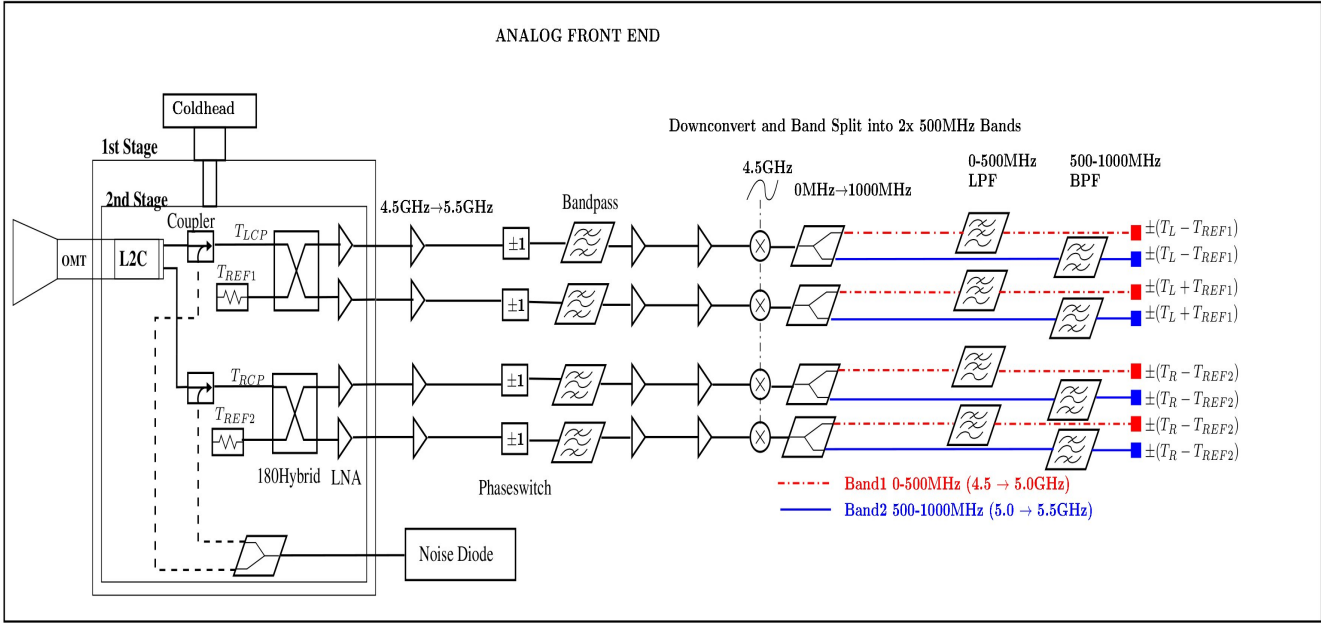


Figure 3.1: Diagram of the analog front end of the digital receiver. There are significantly fewer analog components than the Northern Hemisphere polarimeter (see Appendix .2, Figure 2). The diagram shows the down-conversion of the 1 GHz band (into two 500 MHz bands) followed by the ADC capture. The digital processing is shown on Figure 3.2

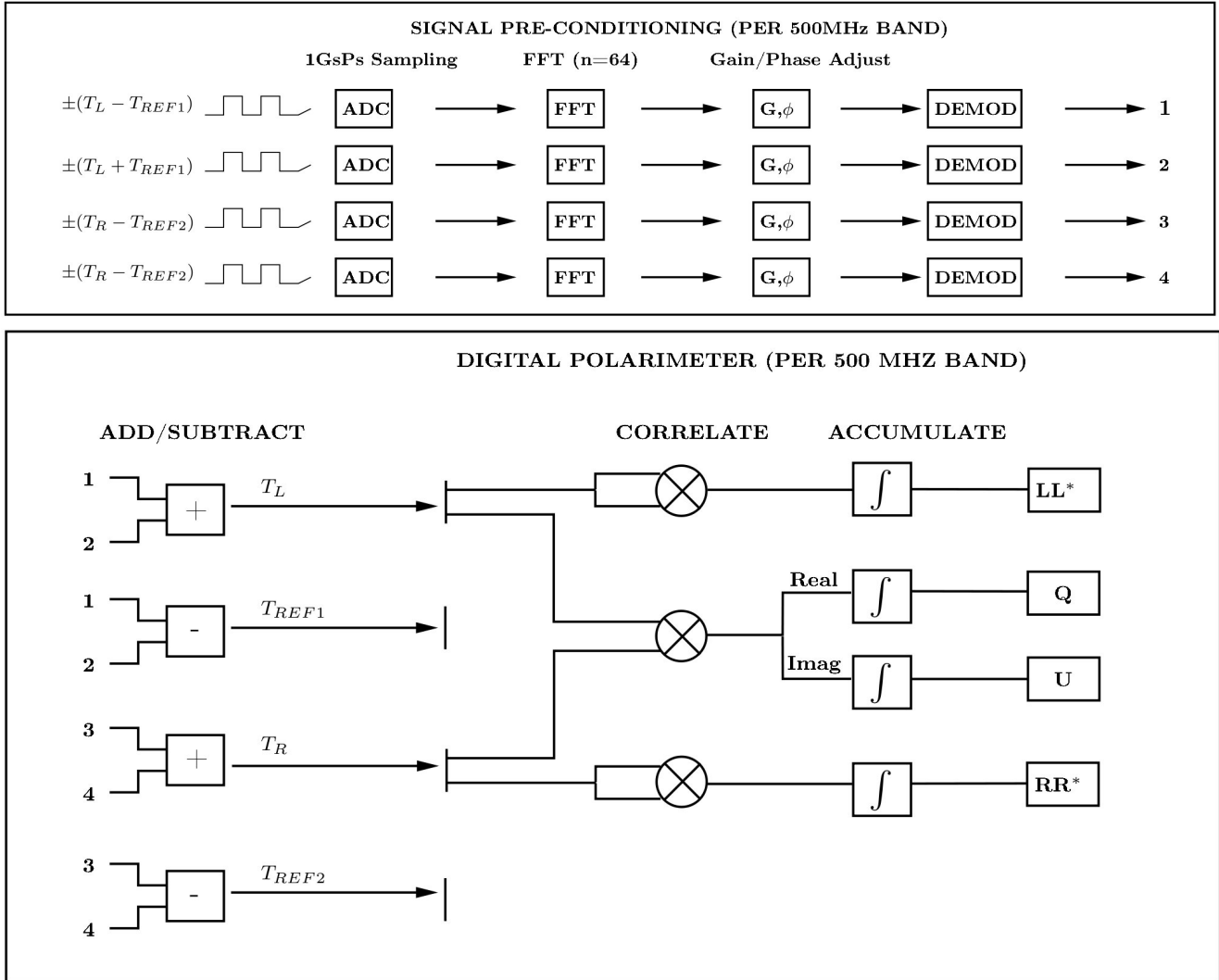


Figure 3.2: Diagram of the digital polarimeter. The diagram shows one of the 500 MHz bands. The signals are sampled, fast-Fourier transformed, gain and phase adjusted, demodulated, added, correlated and then accumulated to produce the values required for the Stokes parameters. See Appendix .1, Equations 1→4 for clarification on the correlations used to produce the Stokes parameters

### 3.1.2 Designs Choices

### 3.1.3 Passive Component Insertion Loss

The system temperature of a radio receiver is given by the Equation 3.1: the Friis Equation.

$$T_{sys} = T_{sky} + T_{spillover} + T_{optics} + \frac{T_{horn}}{G_{optics}} + \frac{T_{passives}}{G_{optics}G_{horn}} + \frac{T_{LNA}}{G_{optics}G_{horn}G_{passives}} \quad (3.1)$$

The continuous-comparison scheme used in the C-BASS receiver is complicated. The receiver requires significant pre-LNA passive components all of which are lossy.

From Equation 3.1 we see that any pre-LNA loss needs to be avoided. It hurts the system, not just in terms of the individual component resistive noise contribution  $(1 - L)T_{phys}$ , but also in terms of the effect these losses have on subsequent components, in particular the LNA noise contribution, where a 3 dB passive loss will increase the effective noise contribution of the LNA by a factor of 2.

RF loss takes one of three forms: resistive losses, mismatch losses, dielectric losses.

Resistive losses hurt the system temperature both by introducing additional noise (proportional to the temperature of the resistor) as well as reducing the signal noise. In a cryogenic radio receiver, losses before the cryostat (warm losses) occur at 300 K while losses inside the cryostat (cold losses) are at the cryogenic operating temperature (for C-BASS South this is 10 K). We can easily see that the 'warm losses' are best avoided.

Mismatch losses occur where there is a slight discontinuity in the impedance of the RF path. Classic examples are RF connectors and RF launches onto substrate. Impedance mismatches, cause reflection of the signal, reducing the signal power. These losses do not result in additional noise themselves, but increase the effective noise figure of the amplifier later in the chain.

Dielectric losses occur due to dissipation of electromagnetic energy in the dielectric (effectively heating the dielectric). The losses are proportional to the frequency of the RF.

In the C-BASS architecture, passive loss is difficult to avoid. Consider for a moment the coaxial interconnects between components. One could be forgiven for assuming that the majority of the cable loss resistive, and thus that cooling a coaxial cable assembly (and thus reducing the resistances) will reduce the total cable assembly insertion loss. However this completely ignores the dielectric loss of a coaxial cable and the mismatch loss of the mated connectors. These are not negligible, and need to be understood.

### Coaxial Cable Insertion Loss Model

Pozar (2005) models the various we expect in a typical coaxial transmission line. Here  $D$  is the diameter of the outer conductor, and  $d$  is the diameter of the inner conductor.

$$\text{Resistance/length} = \left( \frac{f\mu_0}{\pi} \right)^{\frac{1}{2}} \left( \frac{(\mu_{R1}\rho_1)^{\frac{1}{2}}}{D} + \frac{(\mu_{R2}\rho_2)^{\frac{1}{2}}}{d} \right) \quad (3.2)$$

$$Z_0 = \frac{138}{\sqrt{\epsilon_R}} \log \left( \frac{D}{d} \right) \quad (3.3)$$

Loss in a coaxial assembly is given by  $\text{Loss} = \text{Resistance}/2Z_0$ , so combining Equation 3.2 and Equation 3.3 we arrive at

$$\text{Loss/length} = \frac{1}{138 \times 2} \left( \frac{\epsilon_R f \mu_0}{\pi} \right)^{\frac{1}{2}} \left( \frac{(\mu_{R1}\rho_1)^{\frac{1}{2}}}{D} + \frac{(\mu_{R2}\rho_2)^{\frac{1}{2}}}{d} \right) \frac{1}{\log \left( \frac{D}{d} \right)} Np/m \quad (3.4)$$

$$(3.5)$$

Insertion loss due to dielectric loss of a TEM wave propagating through a coaxial cable as

$$\alpha_d = \frac{\pi \epsilon_r \tan \delta}{\lambda} Np/m \quad (3.6)$$

Another, often omitted loss of a cable assembly, is the connector loss. A typical mated SMA

connector has  $0.03\sqrt{f_{GHZ}}$  dB loss. Measuring the passive components in the cryostat requires careful thought. The 24-hour turnaround between measurements is time intensive and careful consideration needs to be taken to optimise measurements.

The test cable assembly requires initial characterisation.

## 3.2 Digital Hardware

### 3.2.1 Roach

### 3.2.2 iADC

The iADC is a multi-purpose CASPER analog-to-digital convertor based around the Atmel/e2V AT84AD001B IC. In non-interleaved mode the ADC is capable of sampling 4 signals at 1GsPs i.e a 500 MHz bandwidth.

#### Power Levels

Tests were carried out to monitor the linearity of the Casper iADC 4-Chann

#### Linearity

#### Van Fleck Corrections

## 3.3 Low Frequency Filters

AS has been explained, the C-BASS is designed for the 4.5→5.5 GHz band. This band is defined using edge-coupled filters early in the RF chain. After suitable RF amplification, the signal is downconverted using a 4.5 GHz LO, mapping 4.5GHz- $\downarrow$ DC and 5.5GHz to 1 GHz. In the digital C-BASS we chose to split this 1 GHz band. One iADC/ROACH would sample the first Nyquist Zone (DC-500MHz) and another would sample the second Nyquist Zone (500-1000MHz). We chose to rely on the earlier edge-coupled filters to define the DC and 1GHz roll-off, and required a suitable 500 MHz low pass filter and 500 MHz high pass filter.

The requirements were small form factor, 20dB roll off in the first 20MHz of band overlap and manufacturability.

### 3.3.1 Filter Design

For the design shown in Figure 3.1, two low frequency filters are required: a 500 MHz lowpass filter and a 500→1000 MHz bandpass filter.

The difficulty of designing filters in the 1GHz frequency range is that it straddles two design regions (Matthaei, G and Young, L and Jones 1980) . Generally higher frequency filters are designed using strip line which scale in size with wavelength making them unsuitable for use at low frequencies. Low frequency designs have tended to use lumped-element capacitors and inductors, but these are notoriously difficult to use at higher frequencies where parasitic effects become important.

The design we have employed uses a lumped-element based approach from with ongoing development and simulations in the *Microwave Office* software suite. Careful use of standardised, well understood, high quality components has allowed us to build filters at unusually high frequencies usually with rapid turnaround times. This makes use of published component values from Murata (Murata 2009)

Results so far are very promising. The 0→500 MHz Low pass filter is complete (see Figure 3.5a) and we are rapidly converging on a suitable band-pass filter for the 500→1000MHz band Figure 3.5b. Our understanding of the behaviour of the Murata components at high frequencies has improved significantly since this version of the bandpass filter.

We focused on using a design/manufacture technique that would allow rapid prototyping of these filters, and allow quick turnaround times for custom filters that might be required in the future. The techniques we have developed allow a custom filter built in a day, with the major bottleneck still being availability of components. This allows significantly more flexible designs to be produced than was the case previously. In addition, the technique opens up the possibility of building compact filters directly onto printed circuit boards using pick and place for mass production. This has potential for use in large scale radio astronomy deployments such as the

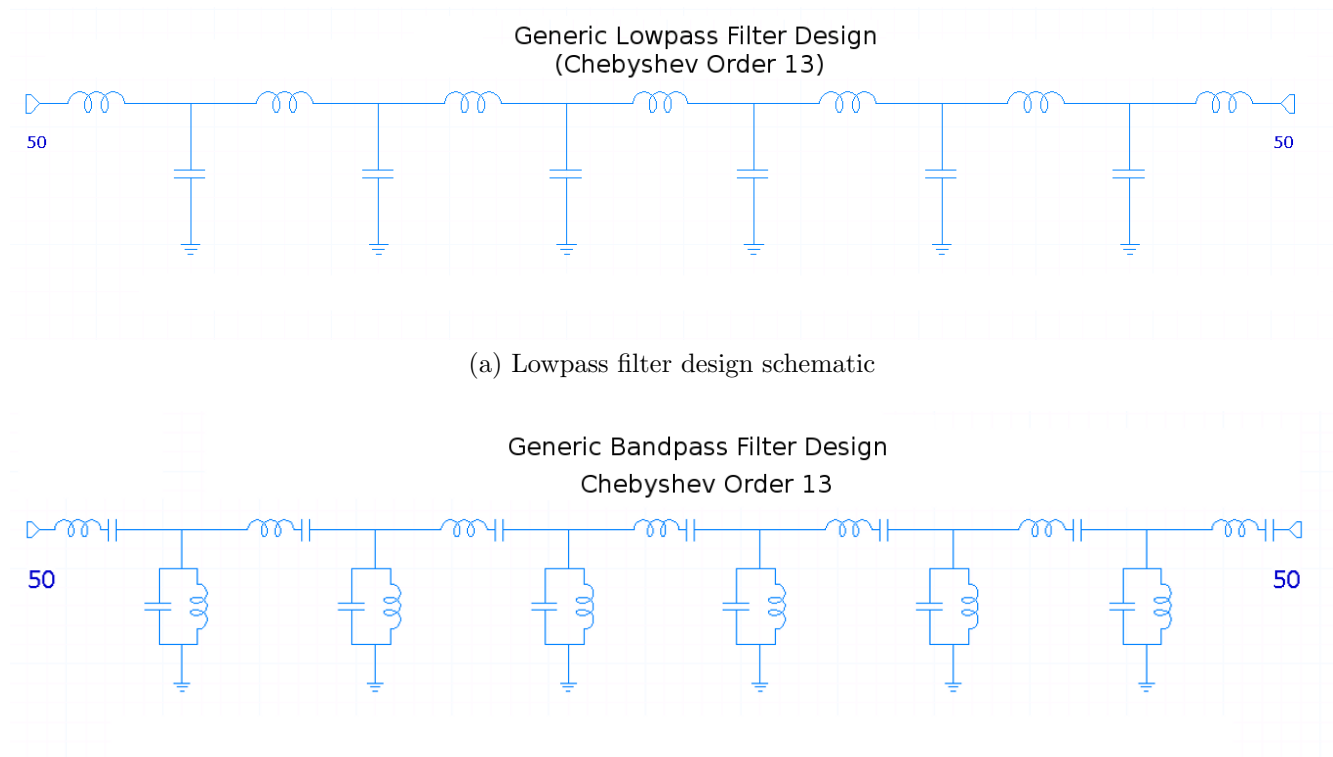


Figure 3.3: Low frequency lumped element filter designs and manufacture

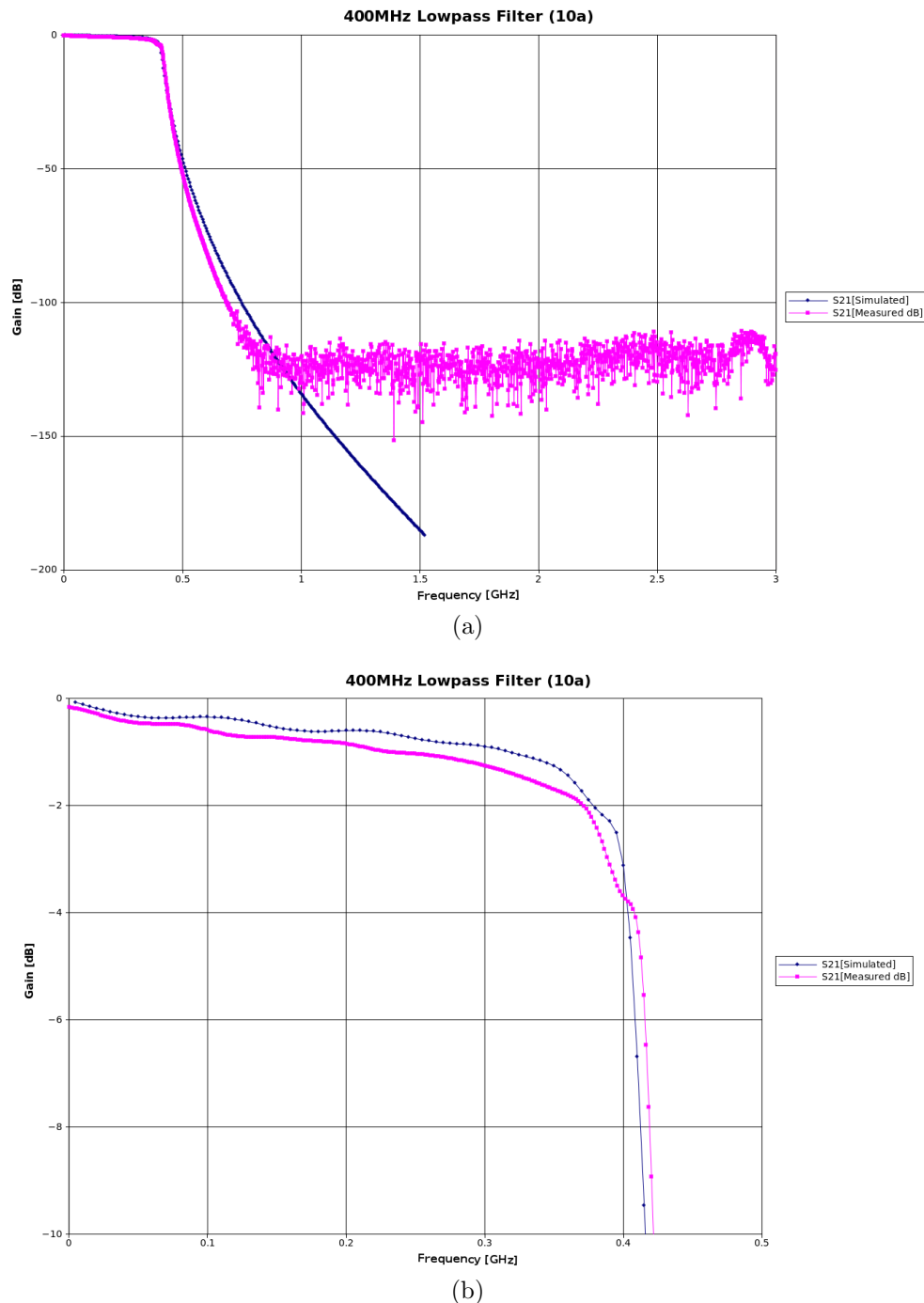


Figure 3.4: Simulated filter performance against measured performance.

Square Kilometer Array.

### 3.3.2 Component Choices

At low frequencies filters are usually designed using surface mount or axial components. At low frequencies parasitic effects are negligible, however at higher frequencies the parasitic inductances and capacitances of the components need to be carefully considered during design.

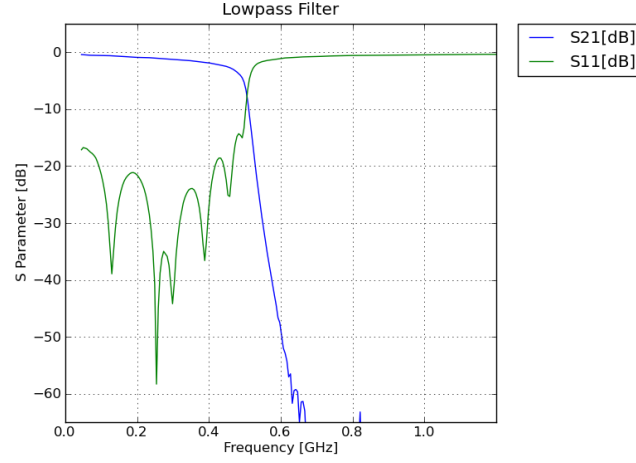
Many manufacturers release component libraries, which quantify these parasitics as well as other parameter changes with frequency. We chose to use Murata components, because of availability of suitable components in low quantities.

Surface mount inductors can present significant challenges at high frequencies. Parasitic capacitance exists due to electric fields between small potential differences between the wire coils, and the wire itself presents a parasitic resistance. We tried the LQW18/LQW15 wire wound type inductors and the LQG18/LQG15 multilayer inductors (Murata 2011). The manufacturing style of both is shown in Figure 3.6. Both provide ranges from  $1\text{nH} \rightarrow 270\text{nH}$  and are designed for use at high frequencies.

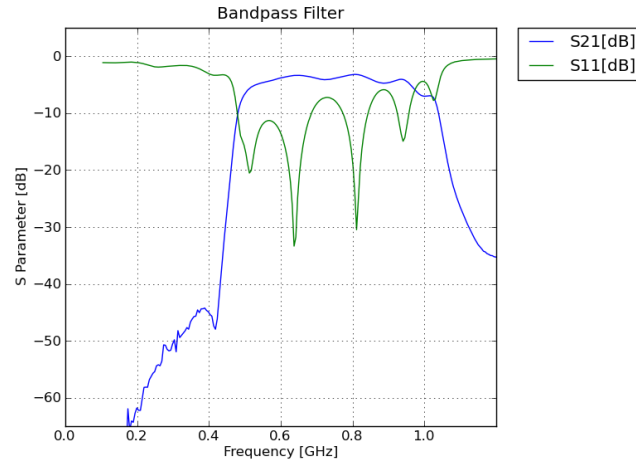
For capacitors we chose the GJM15 Series ceramic capacitors also from Murata (Murata n.d.). These are specifically designed for high frequency operations (up to 10 GHz), and are readily available across the full range of values from  $0.1\text{pF} \rightarrow 33\text{pF}$ . They feature low ESR (parasitic series resistance) (see (Murata n.d.) for values)

### 3.3.3 Manufacture Techniques and Packaging

Component choice is an important consideration, as is symmetry in the design. We have used coplanar waveguide to allow access to the ground plane on the top side of the board, and have laid out the components in a symmetrical fashion. As can be seen in Figure 3.7, careful consideration



(a) The  $0 \rightarrow 500\text{MHz}$  Low pass filter.



(b) The  $1000\text{ MHz}$  low pass filter

Figure 3.5: The 500 MHz lowpass filter and the  $500 \rightarrow 1000\text{MHz}$  bandpass filter. Since the bandpass filter operates at high frequencies where lumped element design is difficult, we decided to make the band pass filter from a cascaded high pass filter (500MHz) and low pass filter (1000MHz). This allowed us to optimise the high end and low end independently. There is still a little work to do on the 1000 MHz filter (i.e the high end of the bandpass filter), but our understanding of these components' behaviours at high frequency has improved significantly, and we believe this will be reflected in the next iteration

# Thesis.ThesisFinal

---

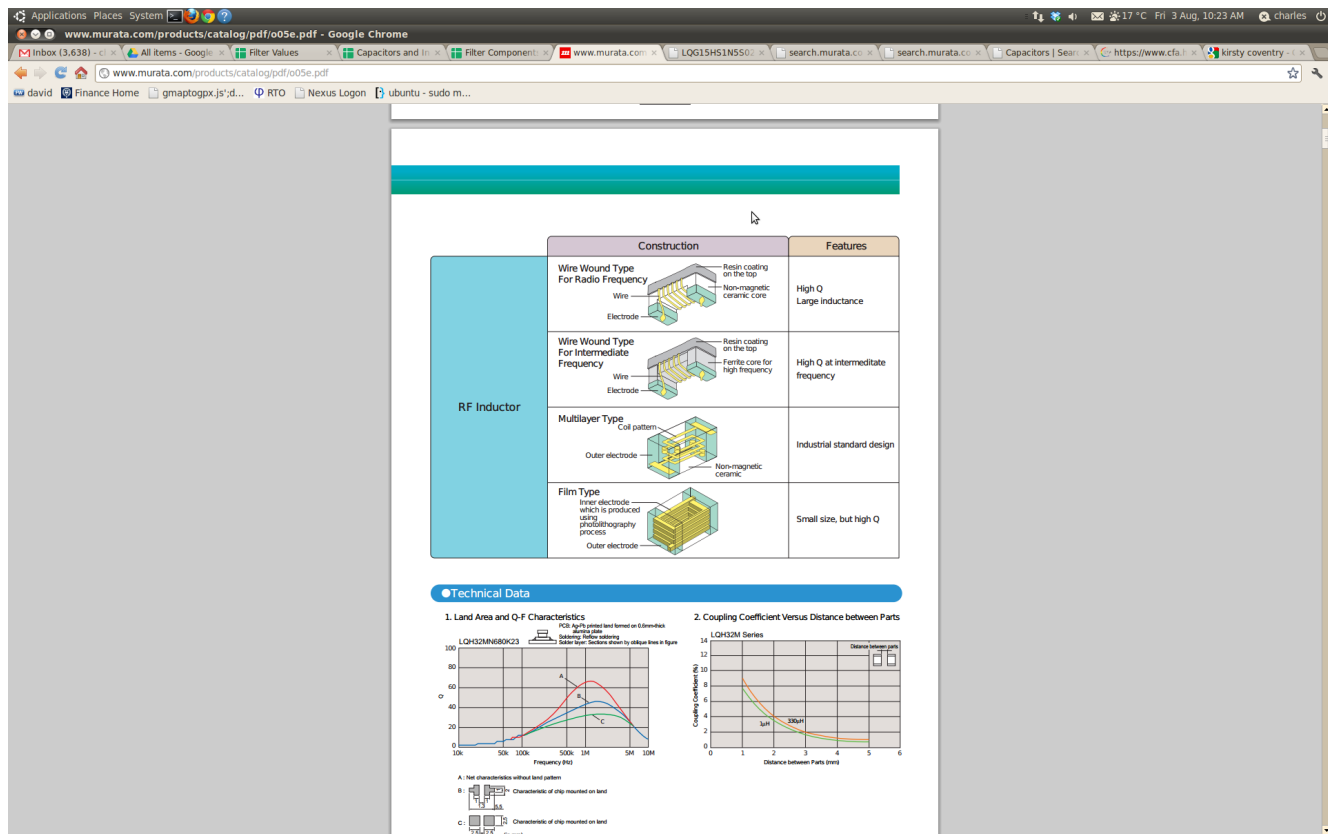


Figure 3.6: Different manufacturing styles of chip inductors (Murata 2011)

also needs to be given to the way in which the filter boards are packaged. The packaging plays an important role in improving the out of band rejection characteristics.

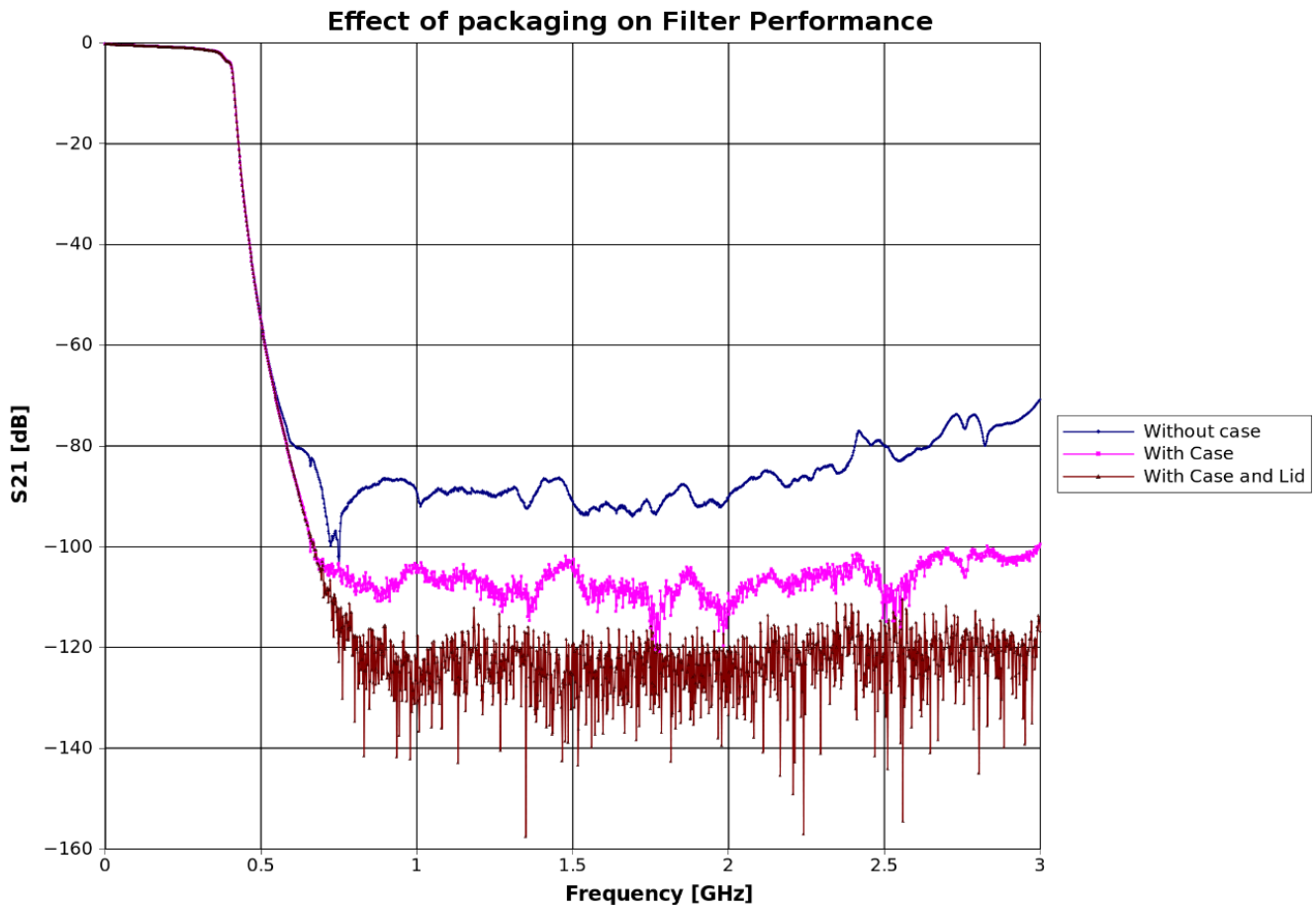


Figure 3.7: Comparison of different stages of the Filter construction process. These plots show the importance of properly enclosing the filter boards

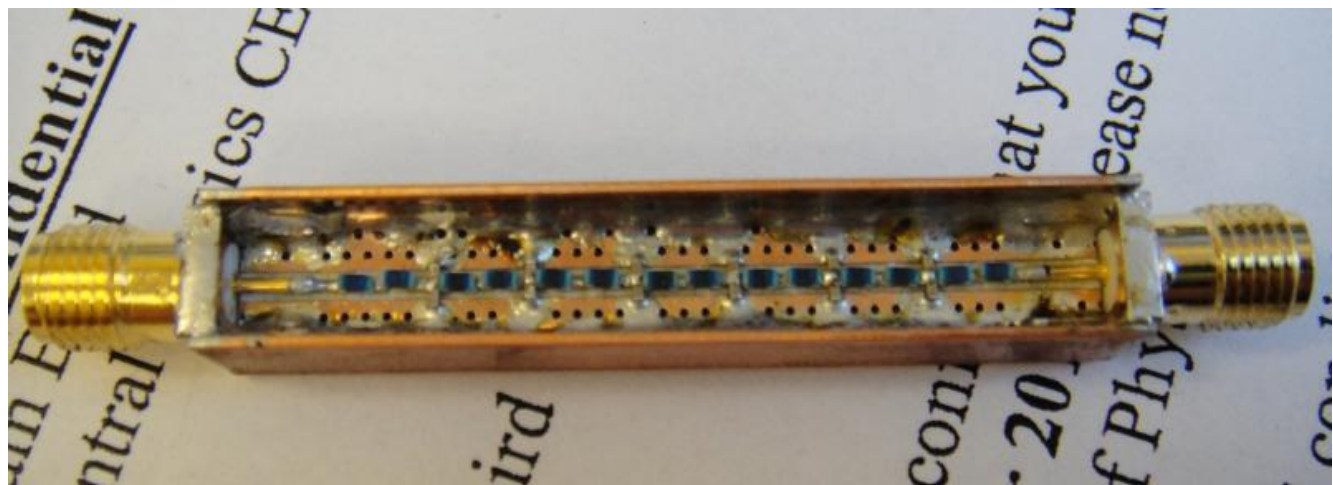


Figure 3.8: Final low frequency filter built into compact box. Notice the symmetry in the placement of components. The complete filter features a copper lid soldered into place completely sealing the unit. We have found that the boxing and lids are very important for optimal filter performance, as is apparent from Figure 3.7. Also notice the solder joint between the PCB and the box wall. This reduces high frequency resonance artifacts, presumably caused by the (otherwise) exposed cavity

### 3.3.4 Performance

## 3.4 Double Sideband Mixers

### 3.4.1 Design and Component Choice

### 3.4.2 Performance

## 3.5 DC-6GHz Amplifiers

Post down conversion gain is required to provide a suitable signal level at the ADC input.

### 3.5.1 Performance

### 3.5.2 Component Choice

### 3.5.3 Wideband Biasing Chokes

### 3.5.4 DC Blocking Capacitors

DC blocking capacitors need to behave like series shorts in the frequency of interest. Capacitors can be modelled as a capacitor in series with a small, parasitic inductance and parasitic resistance (Urs & Rangu 2011, Fiore 2001, Cain 2010). The impedance is then given by the equation in Equation 3.7. This needs to be low (typically less than 1 ohm) across the frequency range of interest.

$$X_{cap} = 1/(2\pi fC) + j2\pi fL + ESR \quad (3.7)$$

Using Equation 3.7 large capacitor values are required for low frequency operation, while high frequency operation is limited by the parasitic inductance.

As an example, at 5 MHz operation, a 100 nF capacitor has a reactance due to capacitance of 0.3 ohms, and a negligible 0.03 ohms contributed by typical parasitic inductances (0603 packaged MLCC capacitor has a typical parasitic inductance of 870 pH (Cain 2010)). However at 6 GHz the situation is reversed. The parasitic inductance now contributes 33 ohms, with the capacitance contribution of 0.0002 ohms being entirely negligible. The parasitic inductance is largely caused by the geometry of the package, with larger packages featuring greater parasitic inductance.

In order to achieve wideband performance from DC to 6 GHz, wideband DC blocking 0402 capacitors from American Technical Ceramics were used (American Technical Ceramics 2012).

The datasheet claims SRF of up to 40 GHz.

### 3.6 Low Noise Amplifier Power Supply

After the decision to move from the Jodrell Bank LNA's to Low Noise Factory LNA's, we required a means of powering the LNA's. Low Noise Factory do supply power supply units, however these do not allow remote monitoring. As such we built our own power supply units, in consultation with Low Noise Factory.

Extensive care was taken in components choice in order to minimise long term bias drifts. Many improvements were made in the original Low Noise Factory design, with particular care being taken to reduce any possible temperature drifts.

The basic schematic of the current source used in the power supply is included in

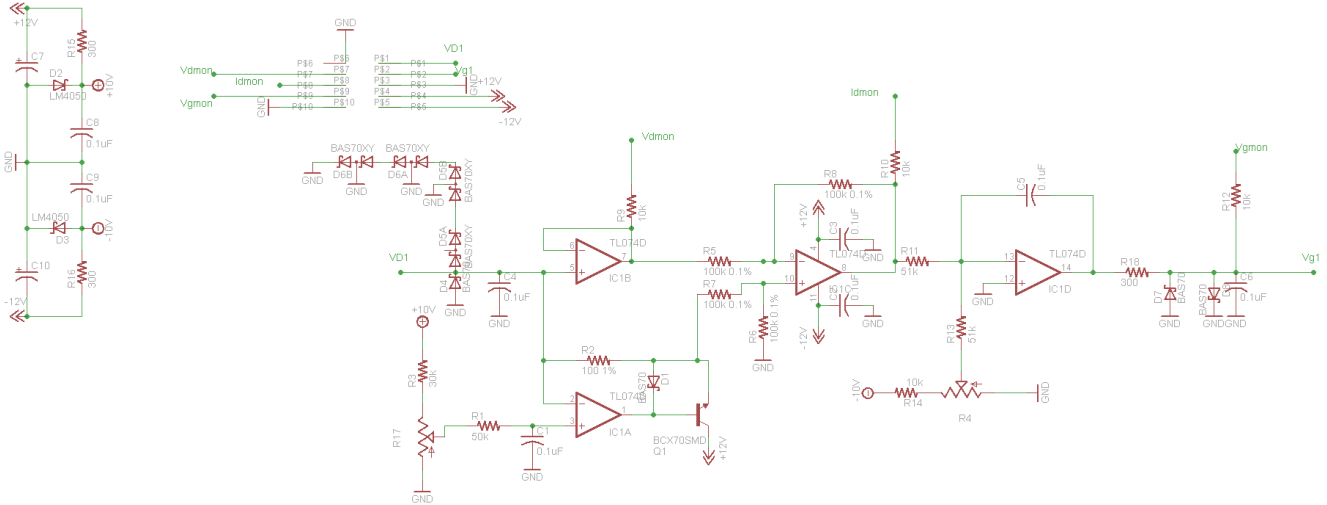
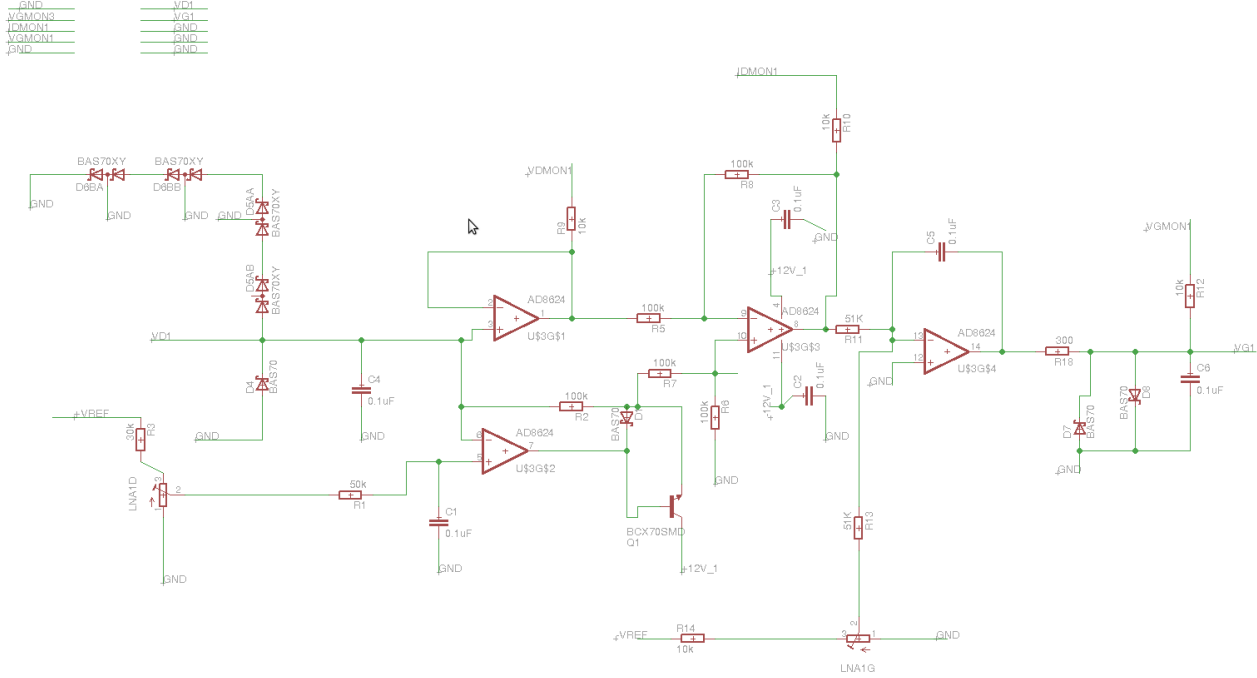
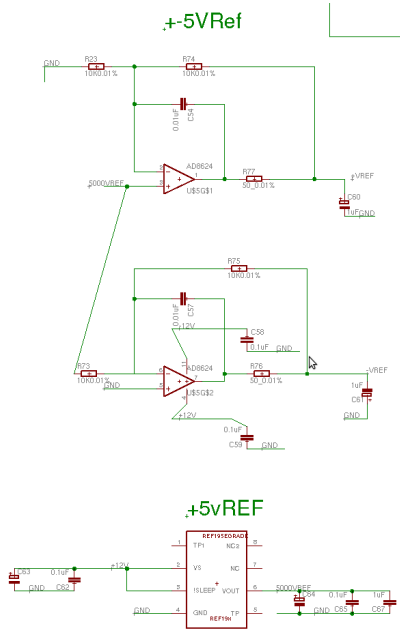


Figure 3.9: The original amplifier power supply schematic.  $\pm 10V$  reference was supplied by LM4050 Zener diode references (thermal stability 50ppm/ $^{\circ}\text{C}$  (Texas Instruments 2011)), and TL074D opamps ( $\text{Vo} \approx 3000\text{uV } \Delta V_{OS}/\Delta C \approx 18\text{uV}/^{\circ}\text{C}$  (Texas Instruments 2005)) were used for the gain and current stages. These were replaced by the more thermally stable REF195 voltage reference (Analog Devices 2011b) and AD8624 opamps (Analog Devices 2011a). Figure 3.10 gives the schematic of the implementation.



(a) New Power supply schematic

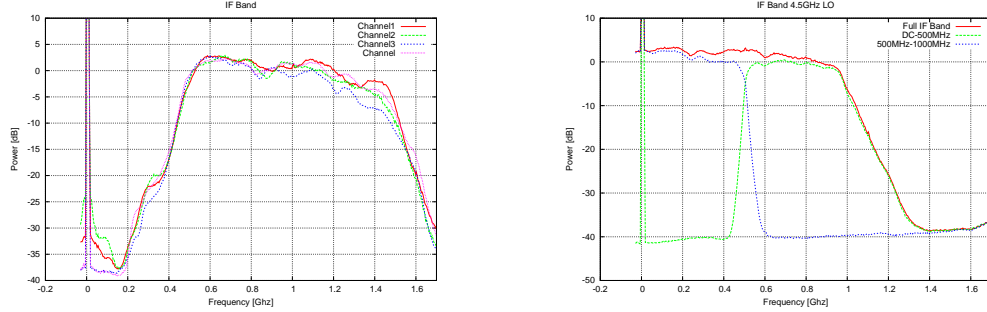


(b) New Reference voltage

Figure 3.10: The updated-LNA Power Supply Board-The  $+5V$  reference voltage is provided by a REF195 E-Grade reference IC with a temperature coefficient of less than  $5\text{ppm}/^\circ\text{C}$  (Analog Devices 2011b). The AD8624 opamps ( $V_o \approx 10\mu\text{V} \Delta V_{OS}/\Delta C \approx 1.2\mu\text{V}/^\circ\text{C}$ ) (Analog Devices 2011a)

Replaced zener diode voltage reference generators, with REF19x units. Zener diodes





(a) Full Band measured by changing to 4GHz LO. This shows the low side rolloff. The steep slope after 1GHz is due to the power splitter frequency response.  
 (b) The two digitised bands, DC→500 MHz and 500→1000 MHz

Figure 4.1: Measurements of the IF Bands digitised by the iADC

## Chapter 4

# Receiver Testing

## 4.1 Introduction

### 4.1.1 Order of Components

## 4.2 Load Stabilisation

### 4.2.1 Cryocontrol

### 4.2.2 Bobbin Redesign

### 4.2.3 Temperature Sensor

# **Chapter 5**

## **The Southern C-BASS System**

C-BASS uses cassegrain optics- We did not know the shape of the primary reflector and needed to establish this.

## 5.1 System Diagram

### 5.1.1 Self-generated RFI considerations

### 5.1.2 Remote Operations

## 5.2 Servo Control

### 5.2.1 Description

Requirements

Hardware

Software Integration

Sensor Hardware Design

Optical Pointing

## 5.3 Primary Dish Profile

### 5.3.1 Photogrammetry

Close range photogrammetry is a fairly recent innovation, which allows highly accurate measurements of large objects to be made in an fast, often automated fashion (Luhmann 2010). Photographs are taken from different angles of targets placed in convenient positions on the object being measured. A few of the targets are geometrically coded (see Figure 5.1), to ease the orientation of multiple photographs in post-processing . The positions of the individual targets can then be determined, with the accuracy varying as a function of camera resolution, target contrast, and separation angle. Accuracies of up to 1:250 000 are routinely quoted when using carefully

calibrated equipment. Fortunately, the technique is suitable for use with high end consumer grade cameras (Deng & Falg 2001), althought the expected accuracy is lowered.

We made use of this technique in order to characterise the donated Telkom dish.

### **Target Choice**

The industry standard is to use retroreflective targets. These generally take the form of black adhesive 'stickers' with reflective sections hand pasted into place. These can be expensive to manufacture and put into position.

In the name of completeness and frugality, we also experimented with a slightly unconventional approach, by projecting a series of targets onto the dish surface from a data projector. As can be seen in Figure 5.1, this allows a higher density distribution of points across the surface, and is significantly less expensive and time consuming to implement.

However this technique suffers from a few obvious limitations, namely resolution and contrast. By fitting centroids to a target position, photogrammetry routinely achieves sub-pixel resolution in the point's position. Poor resolution and low contrast adversely effect this process, to such an extent that we were unable to get a well constrained solution using the projected targets, and after many less than glamourous nights, decided to use the industry standard retroreflective targets.

### **Primary Shape**

The primary surface is not a 'strict' paraboloid, but rather falls into the category of 'shaped optics'. This type of design features an offset from the traditional parabolic reflector described in detail in Galindo (1964), and is a technique used to optimise the aperture efficiency of antennas.

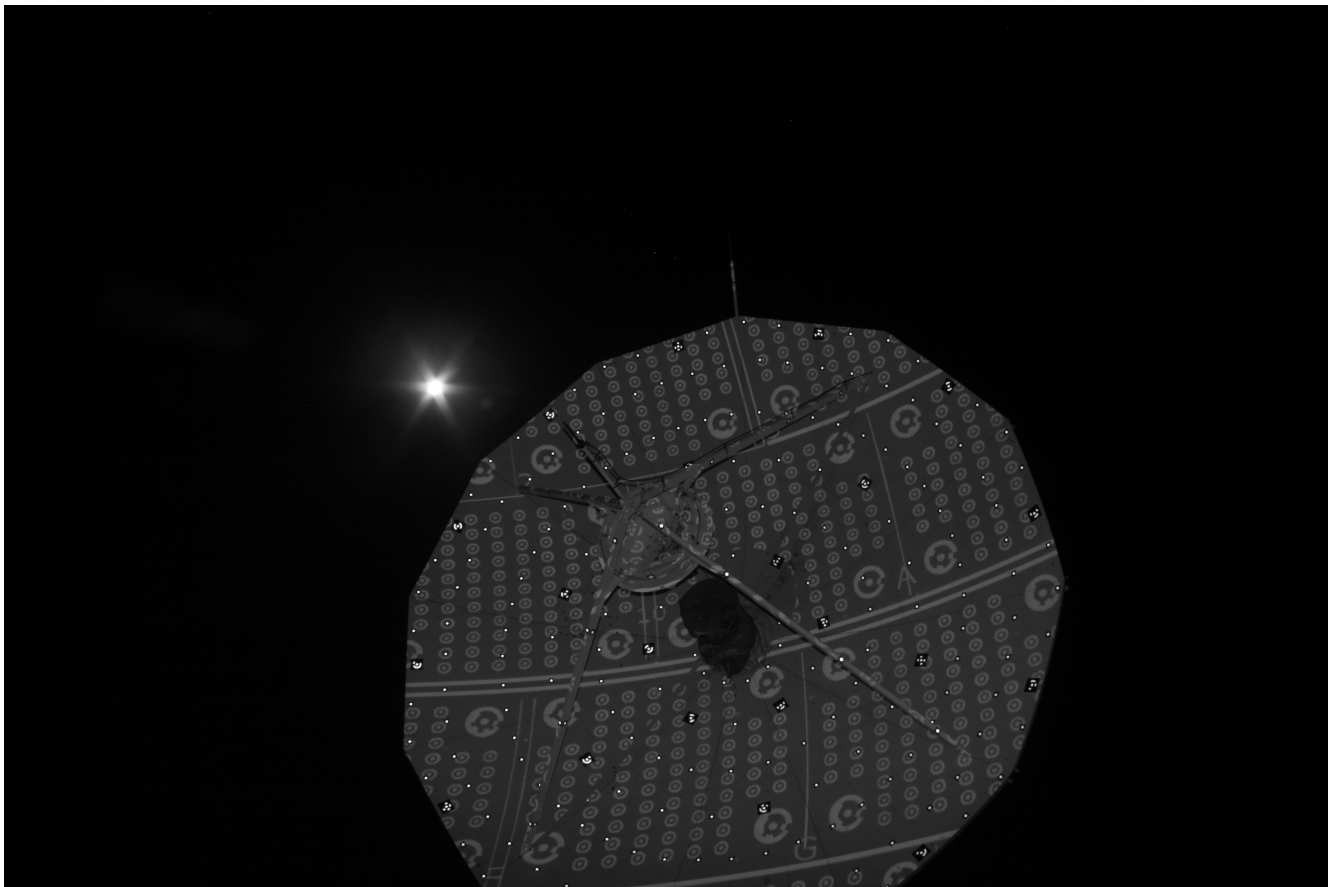


Figure 5.1: An example of a photograph taken of the dish surface. The high contrast, bright points are retroreflective targets, while the other (more densely distributed) points were projected onto the dish from a data projector. The targets consist of both standard circular targets, and geometrically coded targets to help in the post-processing photograph orientation.

### Transportation Quality Control

#### Independent Check of Photogrammetry and First Light

We used a modified 12 GHz receiver and custom designed rectangular feed horn (Meeks 1976) to observe powerful Ku Band Geostationary Satellites. A photograph of the assembled receiver is included in Figure 5.3. It is possible to establish a focal point by scanning through a source and adjusting the position of the feed to maximise the observed power. At the position of maximum received power, the phase centre of the feed and the focal point of the antenna are coincident,

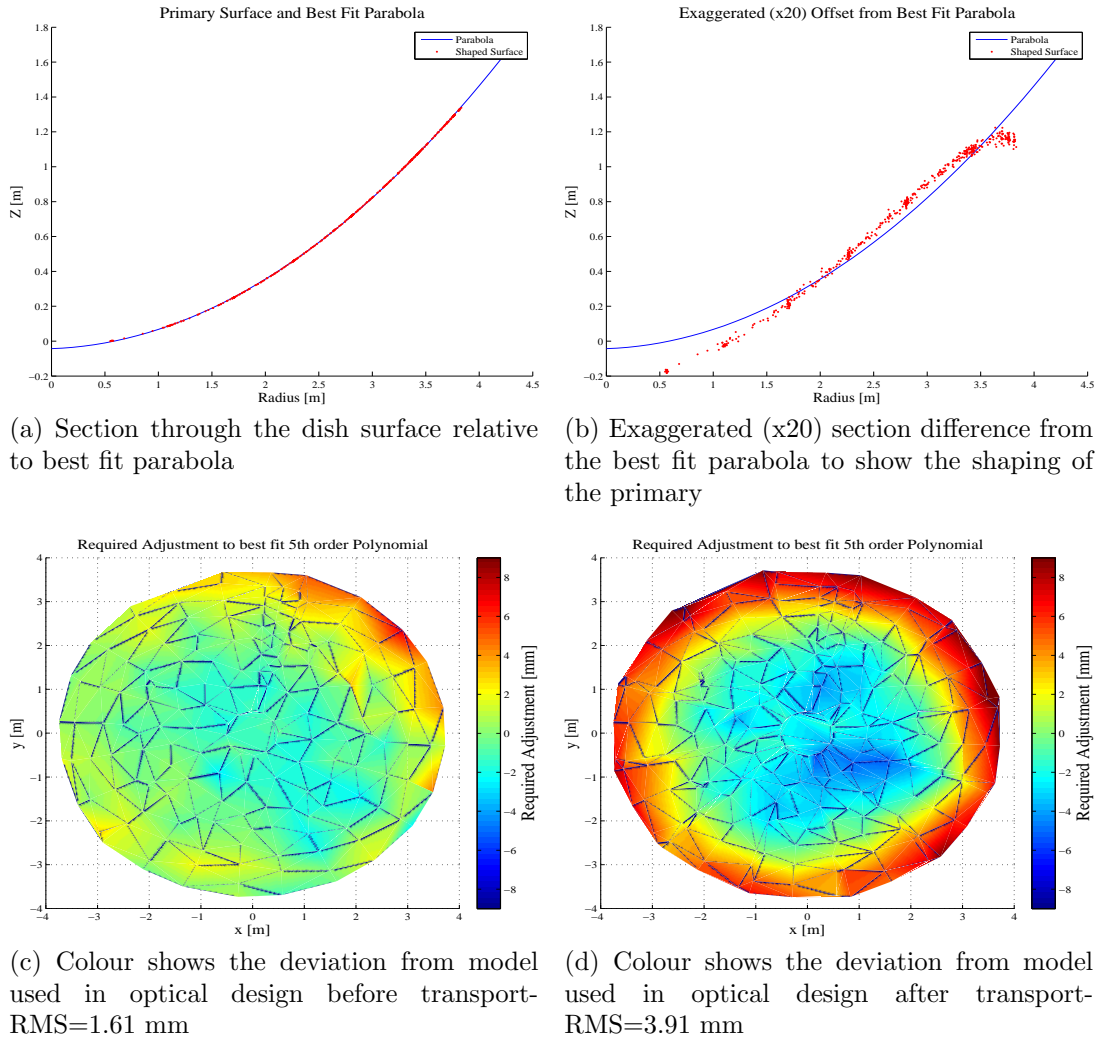


Figure 5.2: Primary reflector offsets from design goal obtained from photogrammetric measurements of the South African 7.6 m dish. The primary shape used in the optical design is a 5th order polynomial fitted to the shape in (a) and (b). The offsets shown in (c) and (d) are with respect to this 5th order polynomial.

providing a direct measurement of the antenna focal point. The results of this experiment are shown in Figure 5.4. It is also possible (using ray tracing) to derive an expected focal point given the photogrammetric shape described in Section 5.3.1. Comparing the measured and expected focal points (derived using the *GRASP8* ray tracing software package), provides an independent check on the quality of the photogrammetry results.

The consistency between expected and measured focal point was very reassuring and confirmed our photogrammetry data. A diagram of the optical layout of the antenna is Figure 5.5

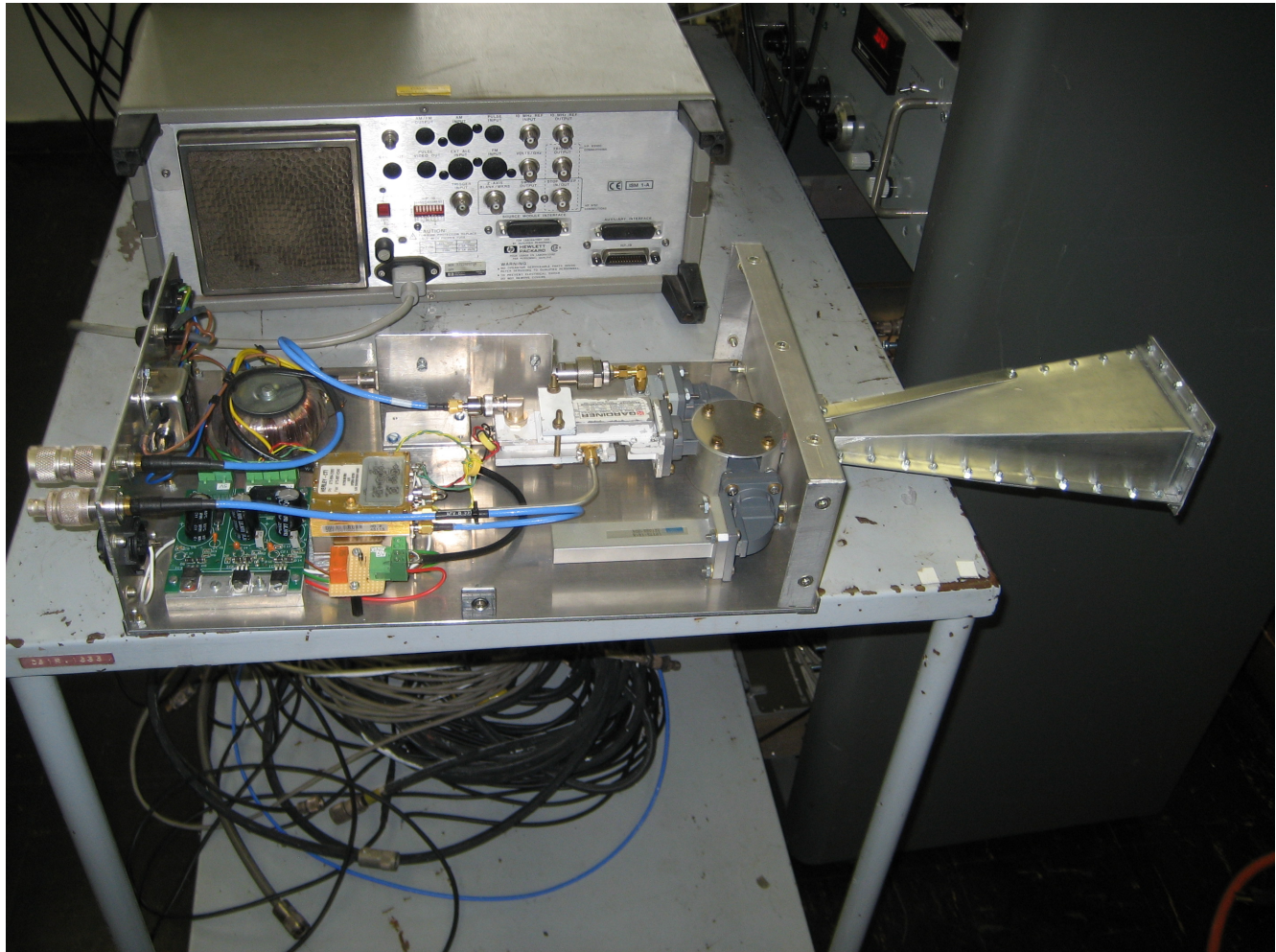


Figure 5.3: 12 GHz Receiver and newly designed feed

## 5.4 Site Establishment

### 5.4.1 Infrastructure

Power Provision

Optical Fibre

Access

Control Shelter Considerations

RFI Survey

### 5.4.2 Science Requirements

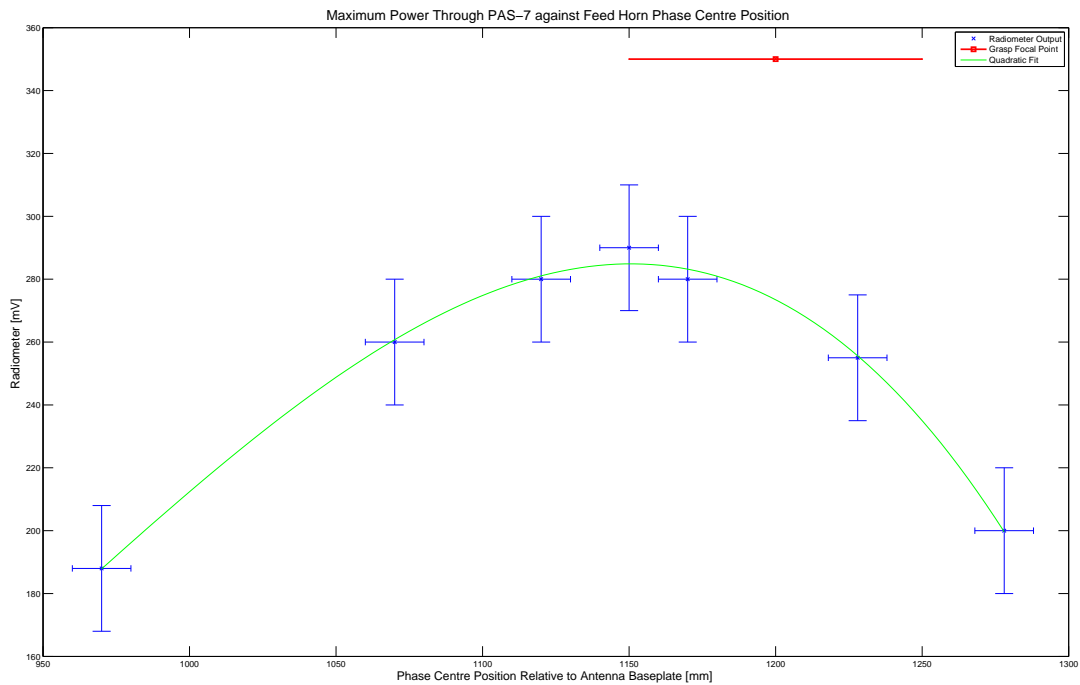


Figure 5.4: Maximum radiometer output voltage (which is proportional to RF power) when scanning through PAS-7, is plotted against feed phase centre position during the scan. The red marker shows the Grasp Software package prediction of the antenna focal point ( $1200 \pm 50$  mm), calculated using the photogrammetry data of the primary and secondary reflector surface shapes. Maximum received power is expected when the feed phase centre and antenna focal point are coincident. The measurements show a maximum power at a feed phase centre position of  $\approx 1150$  mm, which is (just) within the uncertainty of the Grasp simulation prediction of the antenna focal point ( $1200 \pm 50$  mm). Since the Grasp focal point is calculated using the photogrammetry data, this provides an independent ‘sanity’ check of the measurements used to design the new optics of the C-BASS antenna.

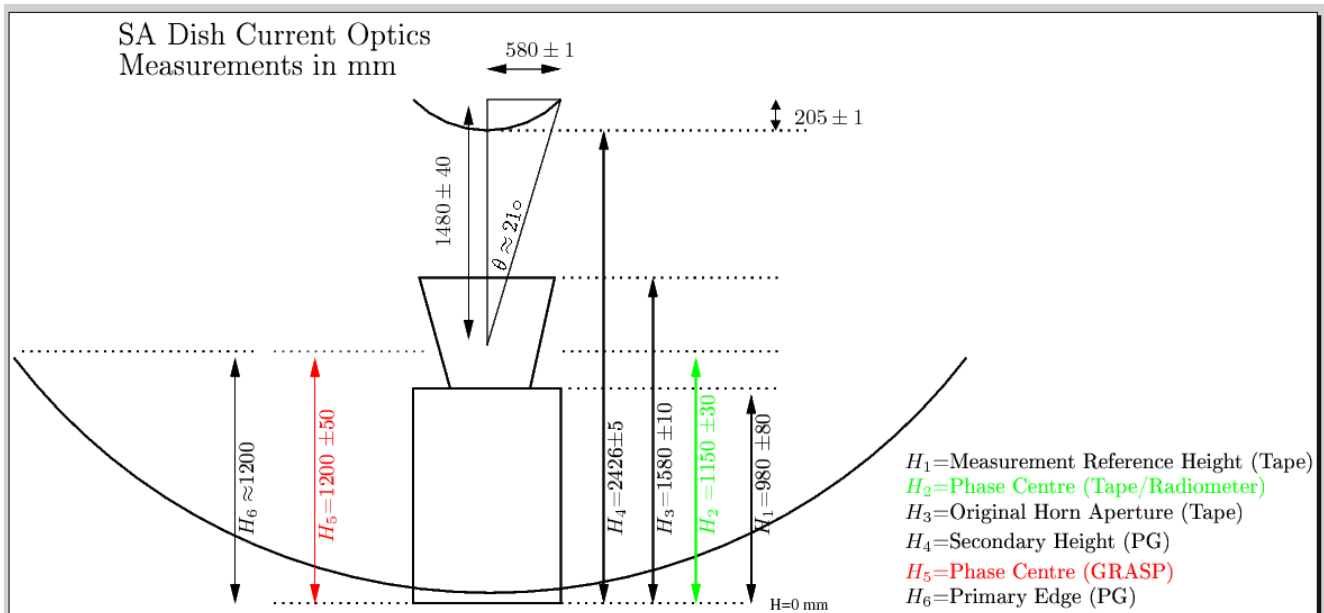


Figure 5.5: Optics of the system before modifications- estimated uncertainties are approximate and not rigorously derived. Note this is the optical configuration prior to the redesign of the optics for the C-BASS experiment. These measurements are confirmed by both photogrammetry and the focal point check described in Section 5.3.1

# **Chapter 6**

## **Deploying the Southern Receiver**

### **6.1 Strategy**

### **6.2 Commissioning Observations**

#### **6.2.1 Beam Patterns**

#### **6.2.2 System Temperature**

#### **6.2.3 Power Spectra**

# **Chapter 7**

## **Preliminary Data (if possible)**

### **7.1 Science Project**

**7.1.1 TBD:Galactic Centre?Spinning Dust Regions? deep CMB fields?**

**7.1.2 Data Reduction**

**7.1.3 Data Analysis**

# **Chapter 8**

## **Conclusions**

**8.1 What's been done**

**8.2 What remains**

## .1 Stokes Parameters

It is important to describe polarisation, as it clarifies key considerations in the receiver design. Tinbergen (1996) provides a good reference on the use of polarimetry in astronomy and was used extensively in the following summary. Detailed descriptions have been avoided.

An electromagnetic wave propagates in a transverse fashion and exhibits vector characteristics. At any instant, the vector describing the electric field can be resolved into two components at right angles to each other. For unpolarised radiation there is no lasting relationship between these two components. For polarised radiation, however, an amplitude and phase relationship does exist, such that the vector comprised of the two components traces out an ellipse, circle or straight line. These three states give rise to the terms *elliptical*, *circular* and *linear* polarisation respectively.

The Stokes parameters (I,Q,U and V) fully describe the state of polarisation. The parameter I characterises the intensity of the incoming radiation, Q and U characterise the state of linear polarisation and V the state of circular polarisation. Measuring I, Q, U and V at radio frequencies can be done by correlating orthogonal modes of the incoming radiation.

Tinbergen (1996) also points out the significant relationship, that left (L) and right (R) hand *circular polarisation* the Stokes parameters are related to the correlations by

$$I = LL^* + RR^* \quad (1)$$

$$Q = 2\text{Re}(LR^*) \quad (2)$$

$$U = -2\text{Im}(LR^*) \quad (3)$$

$$V = LL^* - RR^* \quad (4)$$

(where  $LL^*$  denotes the auto-correlation of the left circular polarisation for example) while for

X and Y *linear polarisations* the parameters relate to the correlations by

$$I = XX^* + RR^* \quad (5)$$

$$Q = XX^* - YY^* \quad (6)$$

$$U = 2Re(XY^*) \quad (7)$$

$$V = 2Im(XY^*) \quad (8)$$

The significance of the equations is apparent when we consider the type of polarisation we are trying to measure. Since Q, U and V will be small percentages, it is preferable to use a form that produces measurements using correlation rather than the less sensitive differencing operation. We can see from the equations that equipment designed for measuring *linear polarisation* (i.e Q and U) should use correlations of circular polarisation (as shown by Equation 2 and Equation 3), while equipment designed for measuring *circular polarisation* (i.e V) should use correlations of linear polarisation (see Equation 8).

For C-BASS we are interested in Galactic polarised emissions. This will be dominated by the synchrotron radiation mechanism (Reich 2006),(Bennett et al. 2003) producing linear polarisation, hence we choose to use correlations of circular polarisation.

## .2 Pseudo-correlation architecture

The polarimeter will be built using a pseudo-correlation architecture (see Figure 1 and Figure 3.2). This is a differential receiver architecture (with continuous comparisons between the sky temperature and a stable reference load, see Figure 1) with the associated benefits of improved stability with amplifier gain fluctuations. Mennella et al. (2003) and Seiffert et al. (2002) describe this

receiver architecture as implemented on the Planck-LFI instrument, and note the improvement over a Dicke switched scheme (i.e switching between load and sky) by avoiding the need for an active switch in the receiver chain and improving the sensitivity by  $\sqrt{2}$ .

We are currently using an analogue pseudo-correlation polarimeter for the OVRO antenna. The receiver consists of a front end cooled to 4 K. The cooled section comprises a ortho-mode transducer (OMT) which separates the incoming signal (defined hereafter as  $T_{sky}$ ) into orthogonal linear polarisations, which are then converted to circular polarisation using  $90^\circ$  hybrids. The reason for the conversion to circular polarisation is described in Appendix .1. Each of the orthogonal circular polarisations (left (LHC) and right (RHC) hand circular polarisation) is then coupled to a reference load signal ( $T_{ref} = 4K$ ) through a  $180^\circ$  hybrid producing two signals ( $T_1 = T_{sky} + T_{ref}$  and  $T_2 = T_{sky} - T_{ref}$ ) which propagate through independent signal paths. In the first signal path, the signal passes through a phase switch applying a delay that alternates between 0 and  $180^\circ$ , while the other signal path is routed through a similar phase switch (for symmetry) with no change in phase being applied. The signals are then recombined (using a  $180^\circ$  hybrid in the Planck architecture) producing the output sequence in Figure 1. The signals are then appropriately correlated to measure the Stokes parameters as described in Section .1. In the new digital receiver the signals will be recombined in the frequency domain, after taking fast-Fourier transforms (FFT) of each of the signals independently. The correlations will then be implemented digitally.

This continuous comparison (again, see Figure 1) between the sky and reference load temperatures is useful for removing gain fluctuations in the amplifiers, since fluctuations will effect both  $T_{sky}$  and the known  $T_{ref}$  equally. In addition, the fast switching reduces the impact of 1/f (or pink) noise in the amplifiers (Seiffert et al. 2002)).

## .3 Digital Implementation

The new digital receiver will perform a similar operation to the analogue receiver and will be implemented on a CASPER *ROACH* board<sup>1</sup>. Two 500 MHz bands will be captured using 1 Gsps analogue-to-digital converters (ADC), after suitable heterodyning of the 4.5 GHz→5.5 GHz frequency band into the 0→1000 MHz band. The two 500 MHz bands are defined by a 0→500 MHz low pass filter (first Nyquist zone) and a 500MHz→1000 MHz band pass filter (second Nyquist zone) as depicted in the diagram in Figure 3.1 and Figure 3.2. A n=128 fast fourier transform (FFT) is performed by the *Virtex-5* field-programmable gate array (FPGA) providing 64 channels ( i.e the real components of the n=128 FFT) and a bin width of 7.8 MHz per channel across each 500 MHz band. Increasing the spectral resolution further would only be possible on a larger FPGA.

### .3.1 Advantages of the Digital Implementation

The analog polarimeter is designed with a single 1 GHz band, with correlations performed using analog components (90 ° and 180 ° hybrids). A similar approach could be used in a digital receiver. The incoming data is sampled, and the analog components emulated with Hilbert transforms and correlating various signals.

Significant improvement on this design can be achieved by performing the correlations in the frequency domain. The incoming signal is fast fourier transformed, and the correlations between signals are implemented as a multiplications. This is the approach we have chosen. The fast fourier transform channelises the data in 8 MHz wide bands, and operations occur on a per-channel basis. This approach is especially useful in radio frequency interference (RFI) detection and rejection. Since RFI is generally very narrow bandwidth ( $\Delta f_{RFI} \ll 8$  MHz), it is unlikely

---

<sup>1</sup><http://casper.berkeley.edu/>

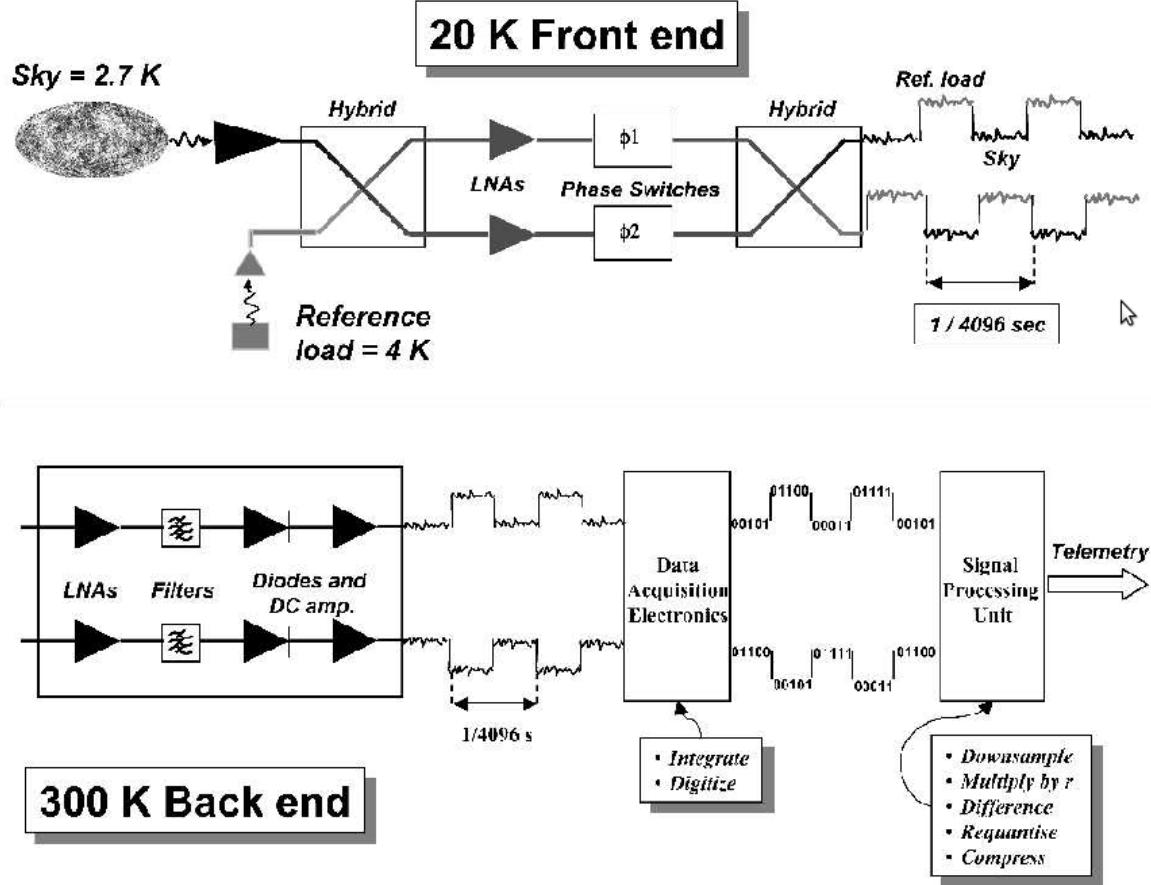


Figure 1: The pseudo correlation architecture (Mennella et al. 2003). The diagram is relevant for one of the orthogonal polarisation states- in the receiver there will be two such signal paths for left and right hand circular polarisation respectively.

to effect more than one of the 8 MHz wide spectral channels and can be robustly detected by a real time spectral kurtosis measurement. The effected channel can be discarded with loss of only 1.5% of the data during the period of the RFI contamination. In comparison, an analogue system requires discarding the entire time series effected by RFI.

Another advantage is the reconfigurability of the digital architecture. A new receiver can be implemented simply and easily, compared to analogue architectures.

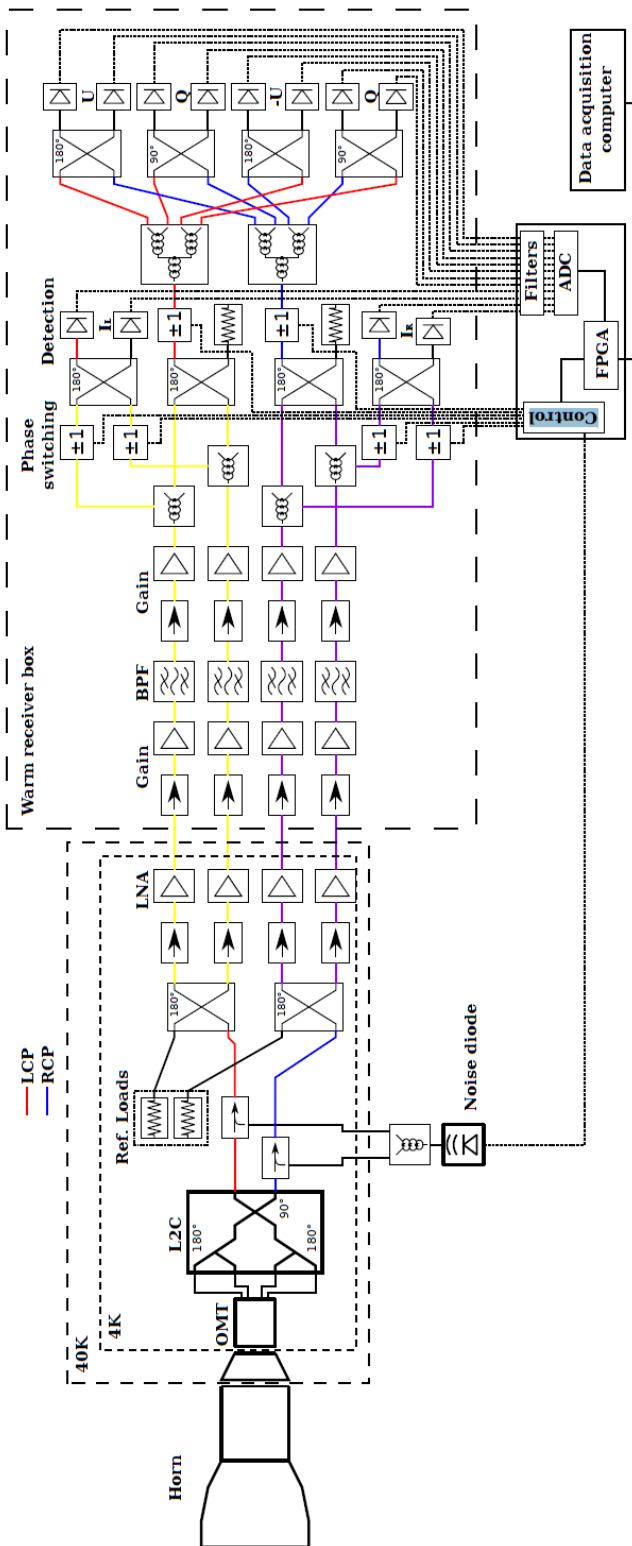


Figure 2: The pseudo-correlation analog C-BASS radiometer/polarimeter designed by Dr. Oliver King and currently installed on the Owens Valley Antenna (King 2009). The  $90^\circ$  phase switch in the front,cold section, converts the linear polarised signal to circular polarised. The signal is then passed through the  $180^\circ$  hybrid, coupling in the load signal and amplified. The signal then splits into the radiometer and polarimeter sections. The radiometer signals are phase switched and passed through a second  $180^\circ$  hybrid producing a signal similar to that illustrated previously in Figure 1. The polarimeter signals are passed through a  $180^\circ$  hybrid to remove the load signal, before phase switching and sampling.

# Bibliography

American Technical Ceramics (2012), ‘ATC550L104 Datasheet’, p. 9001.

**URL:** [http://www.atceramics.com/atc550\\_datasheet.html](http://www.atceramics.com/atc550_datasheet.html)

Analog Devices (2011a), AD8624 Datasheet, Technical report, Analog Devices.

**URL:** [http://www.analog.com/static/imported-files/data\\_sheets/AD8622\\_8624.pdf](http://www.analog.com/static/imported-files/data_sheets/AD8622_8624.pdf)

Analog Devices (2011b), REF19x Series, Technical report, Analog Devices.

**URL:** [http://www.analog.com/static/imported-files/data\\_sheets/REF19xSeries.pdf](http://www.analog.com/static/imported-files/data_sheets/REF19xSeries.pdf)

ArmitageCaplan, C. (2011), ‘Largescale polarized foreground component separation for Planck’, *Monthly Notices of ...* **000**(March).

**URL:** <http://onlinelibrary.wiley.com/doi/10.1111/j.1365-2966.2011.19307.x/full>

Barkats, D., Bischoff, C., Farese, P., Gaier, T., Gundersen, J. O., Hedman, M. M., Hyatt, L., McMahon, J. J., Samtleben, D., Staggs, S. T., Stefanescu, E., Vanderlinde, K. & Winstein, B. (2005), ‘Cosmic Microwave Background Polarimetry Using Correlation Receivers with the PIQUE and CAPMAP Experiments’, *The Astrophysical Journal Supplement Series* **159**(1), 1–26.

**URL:** <http://stacks.iop.org/0067-0049/159/i=1/a=1>

Bennett, C., Hill, R., Hinshaw, G., Nolta, M., Odegard, N., Page, L., Spergel, D., Weiland, J., Wright, E., Halpern, M. & Others (2003), ‘First-year Wilkinson microwave anisotropy probe (WMAP) observations: foreground emission’, *The Astrophysical Journal Supplement Series* **148**, 97.

**URL:** <http://iopscience.iop.org/0067-0049/148/1/97> <http://www.springerlink.com/index/U7N188241NX16>

Cain, J. (2010), Parasitic Inductance of Multilayer Ceramic Capacitors, Technical report, AVX.

**URL:** [www.avx.com/docs/techinfo/parasitic.pdf](http://www.avx.com/docs/techinfo/parasitic.pdf)

Condon, J. (n.d.), ‘Continuum Observations’.

Delabrouille, J. & Cardoso, J. (2009), *Data Analysis in Cosmology*, Vol. 665 of *Lecture Notes in Physics*, Springer Berlin Heidelberg, Berlin, Heidelberg.

**URL:** <http://www.springerlink.com/index/10.1007/978-3-540-44767-2>

- Deng, G. & Falg, W. (2001), ‘An Evaluation of an Off-the-shelf Digital Close- Range Photogrammetric Software Package’, **67**(2), 227–233.
- Dunkley, J., Spergel, D. N., Komatsu, E., Hinshaw, G., Larson, D., Nolta, M. R., Odegard, N., Page, L., Bennett, C. L., Gold, B., Hill, R. S., Jarosik, N., Weiland, J. L., Halpern, M., Kogut, a., Limon, M., Meyer, S. S., Tucker, G. S., Wollack, E. & Wright, E. L. (2009), ‘Five-Year Wilkinson Microwave Anisotropy Probe ( Wmap ) Observations: Bayesian Estimation of Cosmic Microwave Background Polarization Maps’, *The Astrophysical Journal* **701**(2), 1804–1813.  
**URL:** <http://stacks.iop.org/0004-637X/701/i=2/a=1804?key=crossref.63c1817d14d523f8ff5d42d28be21168>
- Fiore, B. R. (2001), Capacitors in Broadband Application, Technical report, American Technical Ceramics.  
**URL:** [http://www.atceramics.com/Userfiles/caps\\_broadbnd\\_apps.pdf](http://www.atceramics.com/Userfiles/caps_broadbnd_apps.pdf)
- Futatsumori, S., Hikage, T. & Nojima, T. (2008), ‘ACLR Improvement of a 5-GHz Power Amplifier Using High-Temperature Superconducting Reaction- Type Transmitting Filters’, *Microwave Conference Proceedings* (October), 1145–1148.
- Galindo, V. (1964), ‘Design of Dual-Reflector Antennas with Arbitrary Phase and Amplitude Distortions’, *IEEE Transactions on Antennas and Propagation* **12**(4), 403–408.
- Garcia-Garcia, J., Bonache, J., Gil, I., Martin, F., Marques, R., Falcone, F., Lopetegi, T., Laso, M. & Sorolla, M. (2005), ‘Comparison of electromagnetic band gap and split-ring resonator microstrip lines as stop band structures’, *Microwave and Optical Technology Letters* **44**(4), 376–379.  
**URL:** <http://doi.wiley.com/10.1002/mop.20640>
- Gold, B., Bennett, C. L., Hill, R. S., Hinshaw, G., Odegard, N., Page, L., Spergel, D. N., Weiland, J. L., Dunkley, J., Halpern, M., Jarosik, N., Kogut, a., Komatsu, E., Larson, D., Meyer, S. S., Nolta, M. R., Wollack, E. & Wright, E. L. (2009), ‘Five-Year Wilkinson Microwave Anisotropy Probe Observations: Galactic Foreground Emission’, *The Astrophysical Journal Supplement Series* **180**(2), 265–282.  
**URL:** <http://stacks.iop.org/0067-0049/180/i=2/a=265?key=crossref.069d33969f0beffa95eb6d970cb64d2>
- Hansen, F. & Banday, A. (2006), ‘Foreground subtraction of cosmic microwave background maps using WI-FIT (wavelet-based high-resolution fitting of internal templates)’, *The Astrophysical Journal* **648**, 784–796.  
**URL:** <http://iopscience.iop.org/0004-637X/648/2/784>
- King, O. (2009), C-BASS: C-Band All-Sky Survey, PhD thesis.
- Leach, S. & Cardoso, J. (2008), ‘Component separation methods for the Planck mission’, *Astronomy & Astrophysics* **615**, 597–615.  
**URL:** <http://arxiv.org/abs/0805.0269>

- Leitch, E. & Kovac, J. (2005), ‘Degree angular scale interferometer 3 year cosmic microwave background polarization results’, *The Astrophysical ...* **900**(Paper I), 10–20.  
**URL:** <http://iopscience.iop.org/0004-637X/624/1/10>
- Luhmann, T. (2010), ‘Close range photogrammetry for industrial applications’, *ISPRS Journal of Photogrammetry and Remote Sensing* **65**(6), 558–569.  
**URL:** <http://linkinghub.elsevier.com/retrieve/pii/S0924271610000584>
- Matthaei, G and Young, L and Jones, E. (1980), *Microwave Filters, Impedance-Matching Networks, and Coupling Structures*, Artech House Publishers.
- Mcmahon, J. J., Samtleben, D., Staggs, S. T., Vanderlinde, K. & Winstein, B. (2005), ‘FIRST MEASUREMENTS OF THE POLARIZATION OF THE COSMIC MICROWAVE BACKGROUND RADIATION’, *The Astrophysical Journal* pp. 1–4.
- Meeks, M. (1976), *Methods of Experimental Physics*, Academic Press.
- Mennella, A., Bersanelli, M., Butler, R., Maino, D., Mandolesi, N., Morgante, G., Valenziano, L., Villa, F., Gaier, T., Seiffert, M. & Others (2003), ‘Advanced pseudo-correlation radiometers for the Planck-LFI instrument’, *Arxiv preprint astro-ph/0307116* (1).  
**URL:** <http://arxiv.org/abs/astro-ph/0307116>
- Murata (2009), ‘Murata Components Library for AWR Microwave Office’.
- Murata (2011), Murata Chip Inductors Datasheet, Technical report, Murata.  
**URL:** <http://www.murata.com/products/catalog/pdf/o05e.pdf>
- Murata (n.d.), GJM High Frequency Ceramic Capacitors, Technical report, Murata.  
**URL:** [http://www.murataamericas.com/murata/murata.nsf/promo\\_ascap\\_gjm.pdf](http://www.murataamericas.com/murata/murata.nsf/promo_ascap_gjm.pdf)
- Pozar, D. (2005), *Microwave Engineering*.
- Readhead, A. C. S., Myers, S. T., Pearson, T. J., Sievers, J. L., Mason, B. S., Contaldi, C. R., Bond, J. R., Bustos, R., Altamirano, P., Achermann, C., Bronfman, L., Carlstrom, J. E., Cartwright, J. K., Casassus, S., Dickinson, C., Holzapfel, W. L., Kovac, J. M., Leitch, E. M., May, J., Padin, S., Pogosyan, D., Pospieszalski, M., Pryke, C., Reeves, R., Shepherd, M. C. & Torres, S. (2004), ‘Polarization observations with the Cosmic Background Imager.’, *Science (New York, N.Y.)* **306**(5697), 836–44.  
**URL:** <http://www.ncbi.nlm.nih.gov/pubmed/15472038>
- Reich, W. (2006), ‘Galactic polarization surveys’.
- Seiffert, M., Mennella, A., Burigana, C., Mandolesi, N., Bersanelli, M., Meinholt, P. & Lubin, P. (2002), ‘1/f noise and other systematic effects in the Planck-LFI radiometers’, *Astronomy and Astrophysics* **391**(3), 1185–1197.  
**URL:** <http://www.edpsciences.org/10.1051/0004-6361:20020880>

Tegmark, M., de Oliveira-Costa, A. & Hamilton, A. (2003), ‘High resolution foreground cleaned CMB map from WMAP’, *Physical Review D* **68**(12), 1–15.  
**URL:** <http://link.aps.org/doi/10.1103/PhysRevD.68.123523>

Texas Instruments (2005), TL074D Datasheet, Technical Report March, Texas Instruments.  
**URL:** <http://www.ti.com/lit/ds/symlink/tl074.pdf>

Texas Instruments (2011), LM4050 / LM4050Q Precision Micropower Shunt Voltage Reference, Technical report, Texas Instruments.  
**URL:** <http://www.ti.com/lit/ds/snoss455d/snoss455d.pdf>

Tinbergen, J. (1996), *Astronomical Polarimetry*, Cambridge University Press.

Urs, B. & Rangu, M. (2011), ‘Estimation of parasitic elements of multilayer ceramic capacitors’, *2011 IEEE 17th International Symposium for Design and Technology in Electronic Packaging (SIITME)* pp. 261–264.  
**URL:** <http://ieeexplore.ieee.org/lpdocs/epic03/wrapper.htm?arnumber=6102731>